Anisotropic elastoplastic response of double-porosity media

Yang Zhao · Ronaldo I. Borja*

Department of Civil and Environmental Engineering, Stanford University, Stanford, CA 94305, USA. *E-mail: borja@stanford.edu

Summary. We present a continuum framework to simulate fluid flow through anisotropic elastoplastic media with double porosity. Two effective stress measures σ' and σ'' emerge from the thermodynamic formulation, which are energy-conjugate to the elastic and plastic components of strain, respectively. Both effective stress measures can be expressed as a combination of the total Cauchy stress σ and the average pore pressure \bar{p} in the two pore scales. In the effective stress for elasticity, \bar{p} is scaled with a rank-2 Biot tensor, whereas the effective stress for plasticity follows the Terzaghi form in which \bar{p} is scaled by the Kronecker delta. The Biot tensor and storage coefficients are derived as functions of elasticity parameters and porosities. A mixed finite element formulation is introduced to discretize the domain and solve initial boundary-value problems. A stabilization scheme is employed on equalorder interpolation for both displacement and pressure fields throughout the entire range of drainage responses. Numerical simulations reproduce the hydromechanical response of Opalinus shale in one-dimensional consolidation tests throughout the range of primary and secondary consolidation under different external loads. Numerical simulations of the consolidation of a rectangular domain subjected to a strip load demonstrate the efficacy of the proposed stabilization scheme, as well as illustrate the impacts of stress history, mass transfer, and different pore systems on the hydromechanical response.

Keywords. Anisotropy, transverse isotropy, double porosity, effective stress, poroplasticity

pore scales

Interface permeability

 \overline{k}

Nomenclature Mass transfer coefficient $\overline{\alpha}$ β $\bar{b}-\phi$, difference between the equivalent Biot coefficient and the Eulerian porosity $\overline{\beta}$ Coefficient that accounts for the solid matrix geometry ϵ_v^p Plastic volumetric strain A scaling coefficient in $\overline{\alpha}$ $\overline{\gamma}$ Permeability coefficient along the axis of anisotropy κ_{\perp} Permeability coefficient along the plane of isotropy κ_{\parallel} κ_m Permeability coefficient in micropores Elastic constants for transversely isotropic material $\lambda, \mu_T, \mu_L, a, b$ $\dot{\lambda}$ Plastic multiplier λ^p Plastic compressibility index Dynamic viscosity of fluid μ_f ϕ Eulerian porosity ϕ^{α} Volume fraction of phase α , $\alpha = s, M, m$ ϕ_{ij} Coefficients in mass balance of fluid, i = M, m; j = M, mFree energy density function ψ^M Fraction of porosity of macropores ψ^m Fraction of porosity of micropores Mass density of the mixture ρ ρ^{α} Partial mass density of phase α , $\alpha = s, M, m$ Intrinsic mass density of phase α , $\alpha = s, M, m$ ρ_{α} Tunable parameter for stabilization θ Bedding plane orientation θ_M Term that is energy-conjugate to \dot{p}_M Term that is energy-conjugate to \dot{p}_m θ_m Term that is energy-conjugate to ψ ζ Characteristic length of the macropores spacing \overline{a} \overline{b} Equivalent Biot coefficient b_{\perp} Biot coefficient along the axis of anisotropy b_{\parallel} Biot coefficient along the plane of isotropy Anisotropy parameters for plasticity, i = 1, 2, 3 c_i Rate of fluid mass transfer from micropores to macropores c_M Rate of fluid mass transfer from macropores to micropores c_m \mathcal{D} Dissipation per unit volume of the mixture \mathcal{D}^p Dissipation triggered by mechanical plastic deformation $\mathcal{D}^{\mathrm{trans}}$ Dissipation triggered by fluid mass transfer across the two

Internal energy per unit total mass of the mixture

| K_{α} | Bulk moduli of phase α , $\alpha = s, M, m$ | | |
|------------------------------------|--|--|--|
| M | Slope of the critical-state line | | |
| \overline{p} | Mean pore pressure weighted by corresponding pore fra | | |
| 1 | tions | | |
| p_{lpha} | Intrinsic pressure of phase α , $\alpha = s, M, m$ | | |
| p_c | Preconsolidation pressure $\alpha, \alpha = s, m, m$ | | |
| p^* | Mean normal alternative stress | | |
| q^* | Deviatoric alternative stress | | |
| $\overset{\iota}{S}_{ij}$ | Storage coefficients, $i = M, m; j = M, m$ | | |
| $oldsymbol{1}$ | Rank-2 symmetric identity tensor | | |
| $\stackrel{-}{lpha}$ | Rank-2 scaling tensor on \overline{p} in the definition of σ' | | |
| $oldsymbol{\chi}_M$ | Term that is energy-conjugate to $\widetilde{\boldsymbol{v}}_M$ | | |
| $oldsymbol{\chi}_m$ | Term that is energy-conjugate to $\widetilde{\boldsymbol{v}}_m$ | | |
| ϵ | Strain tensor | | |
| $oldsymbol{\epsilon}^e$ | Elastic strain tensor | | |
| $m{\epsilon}^p$ | Plastic strain tensor | | |
| $\widetilde{m{\epsilon}}$ | Alternative strain tensor | | |
| $\widetilde{m{\epsilon}}^e$ | Alternative elastic strain tensor | | |
| $\widetilde{m{\epsilon}}^p$ | Alternative plastic strain tensor | | |
| $oldsymbol{\kappa}_M$ | Intrinsic permeability tensor in macropores | | |
| $oldsymbol{\kappa}_m$ | Intrinsic permeability tensor in micropores | | |
| $oldsymbol{\pi}^{lpha}$ | Body force vector exerted on phase α , $\alpha = s, M, m$ | | |
| σ | Total Cauchy stress | | |
| $oldsymbol{\sigma}'$ | Effective stress measure for elasticity | | |
| $oldsymbol{\sigma}^{\prime\prime}$ | Effective stress measure for plasticity | | |
| $\mathring{\boldsymbol{\sigma}}'$ | Zaremba-Jaumann rate of the effective stress σ' | | |
| $oldsymbol{\sigma}^*$ | Alternative stress tensor to define the anisotropic yield sur- | | |
| | face | | |
| $\boldsymbol{\sigma}^{\alpha}$ | Partial stress tensor of phase α , $\alpha = s, M, m$ | | |
| $oldsymbol{\sigma}_{lpha}$ | Intrinsic stress tensor of phase α , $\alpha = s, M, m$ | | |
| \boldsymbol{b} | Rank-2 Biot tensor | | |
| $\overline{oldsymbol{c}}$ | Contribution from fluid mass transfer to the linear mo | | |
| | tum of the mixture | | |
| $oldsymbol{d}$ | Rate of deformation tensor | | |
| \boldsymbol{d}^e | Elastic part of the rate of deformation tensor | | |
| \boldsymbol{d}^p | Plastic part of the rate of deformation tensor | | |
| $oldsymbol{g}$ | Gravitational acceleration vector | | |
| \ddot{l} | Spatial velocity gradient tensor | | |
| m | Microstructure tensor | | |
| $m{n}$ | Normal vector to the bedding plane | | |
| $oldsymbol{q}_M$ | Darcy flux through macropores | | |
| $oldsymbol{q}_m$ | Darcy flux through micropores | | |
| $oldsymbol{s}^*$ | Deviatoric part of the alternative stress tensor | | |

| $oldsymbol{v}_{lpha}$ | Velocity of phase α , $\alpha = s, M, m$ |
|---------------------------|---|
| $\widetilde{m{v}}_{lpha}$ | Relative velocity of phase α respect to the solid phase, |
| | $\alpha = s, M, m$ |
| $oldsymbol{w}$ | Spin tensor |
| \mathbb{C}^e | Elastic moduli tensor |
| ${\mathbb I}$ | Rank-4 symmetric identity tensor |
| \mathbb{P} | Projection tensor to construct σ^* |

1 Introduction

Various theoretical frameworks have been proposed in recent years to solve the coupled problem of solid deformation and fluid flow in porous media with double porosity [1, 9, 42, 61, 62, 64, 72, 79, 87, 102, 103, 108, 118]. Most of these frameworks are only designed for problems with an isotropic elastic solid matrix. Even then, there has been significant disagreement on the theoretical formulation of the problem, particularly with the definition of the effective stress [33]. Among the formulations, Borja and Koliji [17] use continuum thermodynamics to derive an effective stress tensor that is energy-conjugate to the rate of deformation of the solid matrix. This paper aims to generalize this framework to account for anisotropy and inelasticity of the solid matrix. Although the proposed framework is fairly general, the intent of the paper is to apply the theory to geomaterials, more specifically, to rocks such as shale, where the stiffness of the solid matrix is comparable to the stiffness of the solid grains.

In geologic materials, poorly cemented bedding planes could be weak spots for the leakage of pore fluids. Connected microcracks embedded along the bedding plane could create flow channels for rocks like shale, which are typically assumed to be transversely isotropic, leading to an anisotropic permeability tensor with the preferred direction along the bed-parallel direction. Laboratory results revealed that for sedimentary rocks with distinct bedding planes, permeability along the bed-parallel direction could be several orders of magnitude higher than that along the bed-normal direction [10, 29, 63, 82]. To account for the anisotropic transport property of transversely isotropic rocks, Zhang et al. [113] proposed a formulation in which the full permeability tensor is constructed from the two permeability components along the bed-normal and bed-parallel directions, along with a microstructure tensor that reflects the orientation of the bedding plane. Apart from the typically connected fissures, rocks such as shale also possess nanometer-scale pores in the matrix with poor connectivity [105, 114]. Fluids in these pores could barely flow, but may discharge and drain into the larger fissures [109]. To describe the gradation of pore systems with distinctive transport properties and fluid flow

mechanisms in a continuum framework, Barenblatt et al. [5] proposed the concept of double porosity in a non-deformable solid matrix.

However, most materials—even rocks—are deformable, and many of them exhibit anisotropic reversible and irreversible deformation behavior [2, 13, 59, 60, 67, 83, 93, 101, 110. Plasticity models are commonly adopted to represent the ductile irreversible deformation behavior of rocks, but they often rely on the assumption of isotropy in both the elastic and plastic responses [7, 8, 19, 43, 44, 77]. Anisotropy in rocks can be traced to the grain responses at the smaller scale, see [18, 20, 99, 100]. To account for material anisotropy in plasticity modeling, Hill [56] extended the von Mises yield criterion to the orthotropic case using six material parameters that scale the second-order stress terms in the yield criterion. Boehler and Sawczuk [12] proposed an approach that takes advantage of isotropic models by substituting a fictitious stress state projected with a rank-4 tensor to the yield criterion. Based on this idea, Nova [81] and Crook et al. [38] extended the Cam-Clay model for transversely isotropic sedimentary rocks using a projection tensor similar to that used in the model by Hashagen and de Borst [55]. Semnani et al. [90] and Zhao et al. [115] also enhanced the modified Cam-Clay model for transversely isotropic rocks with a three-parameter projection tensor. This latter model was further enriched by Borja et al. [22] to include viscoplasticity and heterogeneity in the mineral distribution in shale rocks. Bryant and Sun [26] also refined this model with micromorphic regularization to accommodate size-dependent anisotropy of geomaterials. More recent works include constructing the anisotropic yield criterion through inelastic homogenization [34, 91].

Laboratory tests also suggest that interstitial fluid pressures may have a significant impact on the yield criterion as well as on the direction of plastic flow [53, 92, 111]. One common approach to incorporate the effect of interstitial fluid pressures into the plasticity model is to substitute the effective stress developed for poroelastic material into the yield criterion [69]. However, whereas this is acceptable for soils where the stiffness of the solid matrix is significantly lower than the stiffness of the solid grains, it lacks a theoretical basis for rocks where the two stiffnesses may be of comparable magnitude. Recently, Zhao and Borja [117] identified two effective stress measures σ' and σ'' that are energy-conjugate to the elastic and plastic components of deformation, respectively. In the effective stress for elasticity, the fluid pressure is scaled with a rank-2 Biot tensor whereas the effective stress for plasticity follows the Terzaghi form [97, 98] in which the fluid pressure is scaled by the Kronecker delta. That an effective stress of the Terzaghi form may be more appropriate to use in the yield criterion has been suspected by numerous authors for quite some time now [24, 58, 70, 86, 96, 111].

In this paper, we use continuum thermodynamics to develop a mathematical framework for coupled solid deformation-fluid flow in anisotropic elastoplastic media with double porosity. Like the formulation of Zhao and Borja [117], two distinct effective stress measures also emerge from the formu-

lation, both of which can be expressed as combinations of the total Cauchy stress σ and a mean pore pressure \bar{p} . In the effective stress for elasticity, \bar{p} is scaled with a rank-2 Biot tensor, whereas the Terzaghi effective stress again follows for plasticity in which \bar{p} is scaled by the Kronecker delta. The proposed framework is then cast into a $u/p_M/p_m$ mixed finite element formulation and later implemented into a code built upon the deal.II Finite Element library [4].

Because of the additional degree of freedom introduced by two fluid pressure terms, it becomes desirable to employ low-order (equal) interpolation for both displacement and pressure fields throughout the entire range of drainage condition, which requires the use of stabilized finite elements [31, 75]. The proposed framework is then calibrated and employed to reproduce the hydromechanical response of Opalinus shale in one-dimensional consolidation tests. Numerical simulations of the consolidation of a rectangular domain under a strip load are also conducted to demonstrate the efficacy of the stabilization scheme utilized in this work, as well as to highlight the impacts of stress history, mass transfer, and different pore systems (either single porosity or double porosity) on the system response.

As for general notations and symbols, we denote symmetric identity tensors of rank 2 and rank 4 by the symbols 1 and \mathbb{I} , respectively. Dot product and double dot product are defined with symbols \cdot and : respectively. Tensor operators \otimes , \oplus , and \ominus are defined such that $(\bullet \otimes \circ)_{ijkl} = (\bullet)_{ij}(\circ)_{kl}$, $(\bullet \oplus \circ)_{ijkl} = (\bullet)_{il}(\circ)_{ik}$, and $(\bullet \ominus \circ)_{ijkl} = (\bullet)_{il}(\circ)_{jk}$.

2 Conservation laws

We adopt mixture theory [23] in the derivation of the governing equations, where the volume of the continuum is decomposed into three phases, including the solid phase, macropores (connected fissures), and micropores (pores within the matrix). The volume fraction occupied by phase α is denoted as ϕ^{α} , and we have

$$\phi^s + \phi^M + \phi^m = 1,\tag{1}$$

where s, M, and m stand for solid, macropores, and micropores, respectively. The overall Eulerian porosity ϕ of the porous medium is the sum of the volume fractions of macropores and micropores, given as

$$\phi = \phi^M + \phi^m. \tag{2}$$

Alternatively, we could also define a binary fraction of porosity as

$$\psi^M = \frac{\phi^M}{\phi}, \qquad \psi^m = \frac{\phi^m}{\phi}, \qquad \psi^M + \psi^m = 1, \tag{3}$$

where ψ^M and ψ^m are the fractions of porosity of macropores and micropores, respectively.

We also define partial mass density of each phase as

$$\rho^s = \phi^s \rho_s, \qquad \rho^M = \phi^M \rho_M, \qquad \rho^m = \phi^m \rho_m, \tag{4}$$

where ρ_s , ρ_M , and ρ_m are the intrinsic densities of solid constituent and pore fluids, respectively. The partial mass density of phase α is the mass of phase α per unit volume of the mixture. The total mass density of the mixture is then given by the sum of the partial mass densities, i.e.,

$$\rho = \rho^s + \rho^M + \rho^m. \tag{5}$$

2.1 Balance of mass

The mass balance equation for each phase in the mixture may be expressed as [17]

$$\frac{d^s \rho^s}{dt} + \rho^s \nabla \cdot \boldsymbol{v}_s = 0, \tag{6a}$$

$$\frac{d^{\alpha} \rho^{\alpha}}{dt} + \rho^{\alpha} \nabla \cdot \boldsymbol{v}_{\alpha} = c_{\alpha}, \quad \alpha = M, m,$$
 (6b)

where $d^{\alpha}(\cdot)/dt$ stands for the material time derivative of variable (\cdot) following the motion of phase α , \mathbf{v}_{α} is the velocity of phase α , c_{M} refers to the rate of fluid mass transfer from micropores to macropores, and c_{m} is the rate of fluid mass transfer from macropores to micropores. For a closed system, we have

$$c_M + c_m = 0. (7)$$

Next, we rewrite all material time derivatives following the motion of the solid phase via the transformation

$$\frac{d^{\alpha}}{dt}(\cdot) = \frac{d}{dt}(\cdot) + \nabla(\cdot) \cdot \widetilde{\boldsymbol{v}}_{\alpha},\tag{8}$$

where $\tilde{\boldsymbol{v}}_{\alpha} = \boldsymbol{v}_{\alpha} - \boldsymbol{v}_{s}$ refers to the relative velocity of phase α with respect to the solid phase, and $d(\cdot)/dt := d^{s}(\cdot)/dt$. We can then write the mass balance equation of each phase following the motion of the solid phase alone,

$$\frac{d\rho^s}{dt} + \rho^s \nabla \cdot \boldsymbol{v} = 0, \qquad (9a)$$

$$\frac{d\rho^{\alpha}}{dt} + \rho^{\alpha} \nabla \cdot \boldsymbol{v} = c_{\alpha} - \nabla \cdot (\rho^{m} \widetilde{\boldsymbol{v}}_{\alpha}), \quad \alpha = M, m,$$
(9b)

where $\boldsymbol{v} := \boldsymbol{v}_s$.

Assuming compressible flow in which the solid and fluids can change in volume, we can write the equations of state for isothermal process in the form [16, 17, 71]

$$f_{\alpha} = f_{\alpha}(p_{\alpha}, \rho_{\alpha}) = 0, \quad \alpha = s, M, m,$$
 (10)

where the p's and ρ 's are the intrinsic pressures and densities of the relevant constituents. The functional relationships stated above imply a one-to-one relationship between the intrinsic pressure and density of each phase, from which we recover the intrinsic bulk relations

$$\frac{d^{\alpha}p_{\alpha}}{dt} = K_{\alpha} \left(\frac{1}{\rho_{\alpha}} \frac{d^{\alpha}\rho_{\alpha}}{dt} \right), \quad \alpha = s, M, m,$$
(11)

where

$$K_{\alpha} = \rho_{\alpha} p_{\alpha}'(\rho_{\alpha}), \quad \alpha = s, M, m$$
 (12)

are the intrinsic bulk moduli of the solid constituent s, fluid constituent in the macropores M, and fluid constituent in the micropores m.

Substituting the definition of partial density $\rho^{\alpha} = \phi^{\alpha} \rho_{\alpha}$ and the derived intrinsic bulk moduli into the mass balance equations (9), we obtain

$$\frac{d\phi^s}{dt} + \frac{\phi^s}{K_s} \frac{dp_s}{dt} + \phi^s \nabla \cdot \boldsymbol{v} = 0, \tag{13a}$$

$$\frac{d\phi^{\alpha}}{dt} + \frac{\phi^{\alpha}}{K_{\alpha}} \frac{dp_{\alpha}}{dt} + \phi^{\alpha} \nabla \cdot \boldsymbol{v} = \frac{c_{\alpha}}{\rho_{\alpha}} - \nabla \cdot \boldsymbol{q}_{\alpha} - \frac{1}{K_{\alpha}} \nabla p_{\alpha} \cdot \boldsymbol{q}_{\alpha}, \qquad (13b)$$

where

$$\mathbf{q}_{\alpha} = \phi^{\alpha} \widetilde{\mathbf{v}}_{\alpha}, \quad \alpha = M, m$$
 (14)

are the Darcy fluxes of fluid through the macropores and micropores, respectively. Further simplification of the mass balance equations requires an evaluation of the intrinsic pressure on the solid constituent p_s [16, 17, 49, 50]. The following section presents a simple strategy to evaluate p_s at the continuum level.

2.2 The Biot tensor and storage coefficients

We recall that the total Cauchy stress tensor σ for double-porosity media can be expressed as the sum

$$\boldsymbol{\sigma} = \boldsymbol{\sigma}^s + \boldsymbol{\sigma}^M + \boldsymbol{\sigma}^m = \phi^s \boldsymbol{\sigma}_s + \phi^M \boldsymbol{\sigma}_M + \phi^m \boldsymbol{\sigma}_m, \tag{15}$$

where σ^s , σ^M , and σ^m are the partial stresses in the solid matrix and fluid matrices in the macropores and micropores, respectively; and σ_s , σ_M , and σ_m are the corresponding intrinsic stress tensors. For isotropic fluids, we can write $\sigma_M = -p_M \mathbf{1}$ and $\sigma_m = -p_m \mathbf{1}$, and so equation (15) specializes to the form

$$\boldsymbol{\sigma} = \phi^s \boldsymbol{\sigma}_s - \phi^M p_M \mathbf{1} - \phi^m p_m \mathbf{1} \equiv \phi^s \boldsymbol{\sigma}_s - \phi \overline{p} \mathbf{1}, \qquad (16)$$

where

$$\overline{p} = \psi^M p_M + \psi^m p^m \tag{17}$$

is the weighted pore fluid pressure in which p_M and p_m are weighted according to the corresponding pore fractions.

Following the formulation for single-porosity media [117], we assume that there exists an effective Cauchy stress tensor σ' that depends solely on the elastic component of deformation in the solid matrix, and write an effective stress equation in the form

$$\sigma = \sigma' - \overline{p}\alpha, \tag{18}$$

where α is a symmetric second-rank tensor. Combining equations (16) and (18) yields

$$\phi^{s} \boldsymbol{\sigma}_{s} = \boldsymbol{\sigma}' + \overline{p}(\phi \mathbf{1} - \boldsymbol{\alpha}). \tag{19}$$

Defining $p_s = -\sigma_s : 1/3$ as the intrinsic solid pressure, we obtain

$$\phi^s p_s = -\frac{1}{3} \mathbf{1} : \boldsymbol{\sigma}' + \beta \overline{p}, \qquad (20)$$

where

$$\beta = \frac{1}{3}\mathbf{1} : \alpha - \phi. \tag{21}$$

Taking the time derivative of equation (20) following the motion of the solid, and noting that $d\phi/dt = -d\phi^s/dt$, we obtain

$$\phi^{s} \frac{dp_{s}}{dt} = (\overline{p} - p_{s}) \frac{d\phi^{s}}{dt} - \frac{1}{3} \mathbf{1} : \dot{\boldsymbol{\sigma}}' + \beta \frac{d\overline{p}}{dt}, \qquad (22)$$

where $\dot{\boldsymbol{\sigma}}' = d\boldsymbol{\sigma}'/dt$.

Next, we substitute (22) into (13a) to obtain

$$(1+\vartheta)\frac{d\phi^s}{dt} + \frac{\beta}{K_s}\frac{d\overline{p}}{dt} - \frac{\mathbf{1} : \dot{\boldsymbol{\sigma}}'}{3K_s} + \phi^s \nabla \cdot \boldsymbol{v} = 0, \qquad (23)$$

where $\vartheta = (\overline{p} - p_s)/K_s$. To explain the physical significance of ϑ , consider a thought experiment in which a dry solid matrix is subjected to a total stress of $\widetilde{\sigma} = \sigma^s + \phi^s \overline{p} \mathbf{1}$. The intrinsic stress in the solid constituent is then given by $\widetilde{\sigma}/\phi^s$ and the intrinsic mean normal stress is $\overline{p} - p_s$. Thus, ϑ is the intrinsic solid volumetric strain when a dry solid matrix is subjected to a hypothetical stress of $\widetilde{\sigma}$. Given the assumption of infinitesimal deformation, $\vartheta \ll 1$, and so expression (23) simplifies to

$$\frac{d\phi^s}{dt} + \frac{\beta}{K_s} \frac{d\overline{p}}{dt} - \frac{\mathbf{1} : \dot{\boldsymbol{\sigma}}'}{3K_s} + \phi^s \nabla \cdot \boldsymbol{v} = 0.$$
 (24)

We now consider the deformation of the solid skeleton through its solid velocity field v. The spatial velocity gradient tensor l, rate of deformation tensor d and the spin tensor w of the solid skeleton are given by the expressions

$$\boldsymbol{l} = \nabla \boldsymbol{v}, \qquad \boldsymbol{d} = \frac{1}{2}(\boldsymbol{l} + \boldsymbol{l}^{\mathsf{T}}), \qquad \boldsymbol{w} = \frac{1}{2}(\boldsymbol{l} - \boldsymbol{l}^{\mathsf{T}}).$$
 (25)

For an elastoplastic material, the rate of deformation tensor d may be decomposed additively into an elastic part and a plastic part,

$$d = d^e + d^p. (26)$$

In the infinitesimal range, the rate of deformation tensor d reduces to the small strain rate tensor $\dot{\epsilon}$.

Consider an objective rate-constitutive equation of the form

$$\dot{\sigma}' = \dot{\sigma}' + \sigma' \cdot w - w \cdot \sigma' = \mathbb{C}^e : d^e, \qquad (27)$$

where $\mathring{\sigma}'$ is the Zaremba-Jaumann rate of the effective stress σ' and \mathbb{C}^e is the elastic moduli tensor. Taking the trace of the expression above and dividing by 3 yields

$$\frac{1}{3}\mathbf{1}: \dot{\boldsymbol{\sigma}}' = \frac{1}{3}\mathbf{1}: \mathbb{C}^e: \boldsymbol{d}^e. \tag{28}$$

Note that $\mathbf{1}: (\boldsymbol{\sigma}' \cdot \boldsymbol{w} - \boldsymbol{w} \cdot \boldsymbol{\sigma}') = 0$. Substituting back into equation (24) yields

$$\frac{d\phi^s}{dt} + \frac{\beta}{K_s} \frac{d\overline{p}}{dt} - \psi : d^e + \phi^s \nabla \cdot v = 0, \qquad (29)$$

where

$$\psi = \frac{\mathbf{1} : \mathbb{C}^e}{3K_s} \,. \tag{30}$$

Next, consider the material time derivatives

$$\frac{d\phi^{\alpha}}{dt} = \frac{d\psi^{\alpha}}{dt}(1 - \phi^{s}) - \psi^{\alpha}\frac{d\phi^{s}}{dt}, \qquad \alpha = M, m.$$
 (31)

Substituting equations (29) and (31) into (13b) yields

$$\frac{d\psi^{\alpha}}{dt}(1-\phi^{s}) + \psi^{\alpha}\left(\frac{\beta}{K_{s}}\frac{d\overline{p}}{dt} - \boldsymbol{\psi}: \boldsymbol{d}^{e} + \frac{\phi}{K_{\alpha}}\frac{dp_{\alpha}}{dt} + \nabla \cdot \boldsymbol{v}\right)$$

$$= \frac{c_{\alpha}}{\rho_{\alpha}} - \nabla \cdot \boldsymbol{q}_{\alpha} - \frac{1}{K_{\alpha}}\nabla p_{\alpha} \cdot \boldsymbol{q}_{\alpha}, \quad \alpha = M, m. \quad (32)$$

We can further simplify the expression by noting that

$$\nabla \cdot \boldsymbol{v} = \boldsymbol{1} : \boldsymbol{d} = \boldsymbol{1} : (\boldsymbol{d}^e + \boldsymbol{d}^p). \tag{33}$$

Substituting back into equation (32) gives

$$\frac{d\psi^{\alpha}}{dt}(1-\phi^{s}) + \psi^{\alpha}\left(\frac{\beta}{K_{s}}\frac{d\overline{p}}{dt} + \frac{\phi}{K_{\alpha}}\frac{dp_{\alpha}}{dt} + \boldsymbol{b}:\boldsymbol{d}^{e} + \boldsymbol{1}:\boldsymbol{d}^{p}\right) \\
= \frac{c_{\alpha}}{\rho_{\alpha}} - \nabla \cdot \boldsymbol{q}_{\alpha} - \frac{1}{K_{\alpha}}\nabla p_{\alpha} \cdot \boldsymbol{q}_{\alpha}, \quad \alpha = M, m, \quad (34)$$

where

$$b = 1 - \psi, \tag{35}$$

is a rank-2 tensor, which we identify as the same Biot tensor introduced by Zhao and Borja [117]. We note, however, that this tensor now appears in the mass balance equations for both the macropore $(\alpha = M)$ and micropore $(\alpha = m)$ fluids.

Lastly, we can expand the material time derivative of the mean pore pressure as

$$\frac{d\overline{p}}{dt} = \psi^M \frac{dp_M}{dt} + p_M \frac{d\psi^M}{dt} + \psi^m \frac{dp_m}{dt} + p_m \frac{d\psi^m}{dt}.$$
 (36)

Substituting this back into equation (34) yields the mass balance equations for the two fluids, which we now display separately for $\alpha = M, m$ as

$$\left(\phi + \widetilde{\phi}_{MM}\right) \frac{d\psi^{M}}{dt} + \widetilde{\phi}_{Mm} \frac{d\psi^{m}}{dt} + \psi^{M} \mathbf{b} : \mathbf{d}^{e} + \psi^{M} \mathbf{1} : \mathbf{d}^{p} + S_{MM} \frac{dp_{M}}{dt} + S_{Mm} \frac{dp_{m}}{dt} = \frac{c_{M}}{\rho_{M}} - \nabla \cdot \mathbf{q}_{M} - \frac{1}{K_{M}} \nabla p_{M} \cdot \mathbf{q}_{M}$$
(37)

and

$$\widetilde{\phi}_{mM} \frac{d\psi^{M}}{dt} + \left(\phi + \widetilde{\phi}_{mm}\right) \frac{d\psi^{m}}{dt} + \psi^{m} \boldsymbol{b} : \boldsymbol{d}^{e} + \psi^{m} \boldsymbol{1} : \boldsymbol{d}^{p}$$

$$+ S_{mM} \frac{dp_{M}}{dt} + S_{mm} \frac{dp_{m}}{dt} = \frac{c_{m}}{\rho_{m}} - \nabla \cdot \boldsymbol{q}_{m} - \frac{1}{K_{m}} \nabla p_{m} \cdot \boldsymbol{q}_{m}, \quad (38)$$

where S_{MM} , S_{mm} , S_{Mm} , and S_{mM} are elements of storage coefficient matrix defined as

$$S_{MM} = \frac{\phi^M}{K_M} + \frac{\psi^M \psi^M \beta}{K_s} \,, \tag{39a}$$

$$S_{mm} = \frac{\phi^m}{K_m} + \frac{\psi^m \psi^m \beta}{K_s} \,, \tag{39b}$$

$$S_{mM} = S_{Mm} = \frac{\psi^M \psi^m \beta}{K_s} \,, \tag{39c}$$

and

$$\widetilde{\phi}_{MM} = \frac{\psi^M \beta p_M}{K_s} \,, \tag{40a}$$

$$\widetilde{\phi}_{mm} = \frac{\psi^m \beta p_m}{K_s} \,, \tag{40b}$$

$$\widetilde{\phi}_{Mm} = \frac{\psi^M \beta p_m}{K_s} \,, \tag{40c}$$

$$\widetilde{\phi}_{mM} = \frac{\psi^m \beta p_M}{K_s} \,. \tag{40d}$$

Observe that some of these coefficients include coupling terms linking variables in the two porosity scales.

2.3 Balance of linear momentum

Mixture theory allows the solid matrix and the fluids in both the macropores and micropores to be treated as individual phases. The balance of linear momentum in the absence of inertia forces can then be written in terms of the partial stresses and mass densities,

$$\nabla \cdot \boldsymbol{\sigma}^s + \boldsymbol{\pi}^s + \rho^s \boldsymbol{g} = \boldsymbol{0} \,, \tag{41a}$$

$$\nabla \cdot \boldsymbol{\sigma}^{\alpha} + \boldsymbol{\pi}^{\alpha} + \rho^{\alpha} \boldsymbol{g} = c_{\alpha} \boldsymbol{v}_{\alpha} , \quad \alpha = M, m ,$$
 (41b)

where π^{α} (for $\alpha = s, M, m$) are the body force vectors exerted on phase α by the other two phases. For a closed system, we must have

$$\sum_{s,M,m} \boldsymbol{\pi}^{\alpha} = \mathbf{0} \,. \tag{42}$$

Summing up the individual momentum equations over all phases yields the balance of linear momentum for the mixture

$$\nabla \cdot \boldsymbol{\sigma} + \rho \boldsymbol{g} = \overline{\boldsymbol{c}},\tag{43}$$

where $\overline{c} := \sum_{M,m} c_{\alpha} \widetilde{v}_{\alpha}$ is the contribution from fluid mass transfer between different pore scales to the linear momentum of the mixture.

2.4 Rate of change of internal energy

Ignoring heat, chemical reaction, etc., and focusing solely on the hydromechanical contributions, the rate of change of internal energy per unit volume of the mixture is given by the expression

$$\rho \dot{e} = \sum_{s,M,m} \boldsymbol{\sigma}^{\alpha} : \boldsymbol{d}_{\alpha} + \frac{1}{2} \sum_{M,m} c_{\alpha} \boldsymbol{v}_{\alpha} \cdot \boldsymbol{v}_{\alpha} , \qquad (44)$$

where e is the internal energy per unit total mass of the mixture, and $\mathbf{d}_{\alpha} = (\nabla \mathbf{v}_{\alpha} + \mathbf{v}_{\alpha} \nabla)/2$. The first term on the right hand side refers to the contribution from mechanical work, whereas the second term represents the influence of fluid mass transfer between the two pore scales. We can also write the above expression in terms of the total Cauchy stress as

$$\rho \dot{e} = \boldsymbol{\sigma} : \boldsymbol{d} - p_M \phi^M \nabla \cdot \widetilde{\boldsymbol{v}}_M - p_m \phi^m \nabla \cdot \widetilde{\boldsymbol{v}}_m + \frac{1}{2} \sum_{M,m} c_\alpha \boldsymbol{v}_\alpha \cdot \boldsymbol{v}_\alpha. \tag{45}$$

Following the formulation in Ref. [17], we note that

$$-\phi^{M} \nabla \cdot \widetilde{\boldsymbol{v}}_{M} = \nabla \phi^{M} \cdot \widetilde{\boldsymbol{v}}_{M} - \nabla \cdot \boldsymbol{q}_{M}$$

$$= \nabla \phi^{M} \cdot \widetilde{\boldsymbol{v}}_{M} + \psi^{M} \boldsymbol{b} : \boldsymbol{d}^{e} + \psi^{M} \boldsymbol{1} : \boldsymbol{d}^{p}$$

$$+ \left(\phi + \widetilde{\phi}_{MM}\right) \frac{d\psi^{M}}{dt} + \widetilde{\phi}_{Mm} \frac{d\psi^{m}}{dt} - \frac{c_{M}}{\rho_{M}}$$

$$+ S_{MM} \frac{dp_{M}}{dt} + S_{Mm} \frac{dp_{m}}{dt} + \frac{1}{K_{M}} \nabla p_{M} \cdot \boldsymbol{q}_{M}$$

$$(46)$$

and

$$-\phi^{m}\nabla\cdot\widetilde{\boldsymbol{v}}_{m} = \nabla\phi^{m}\cdot\widetilde{\boldsymbol{v}}_{m} - \nabla\cdot\boldsymbol{q}_{m}$$

$$= \nabla\phi^{m}\cdot\widetilde{\boldsymbol{v}}_{m} + \psi^{m}\boldsymbol{b}:\boldsymbol{d}^{e} + \psi^{m}\boldsymbol{1}:\boldsymbol{d}^{p}$$

$$+ \widetilde{\phi}_{mM}\frac{d\psi^{M}}{dt} + \left(\phi + \widetilde{\phi}_{mm}\right)\frac{d\psi^{m}}{dt} - \frac{c_{m}}{\rho_{m}}$$

$$+ S_{mM}\frac{dp_{M}}{dt} + S_{mm}\frac{dp_{m}}{dt} + \frac{1}{K_{m}}\nabla p_{m}\cdot\boldsymbol{q}_{m}$$

$$(47)$$

after substituting the expression for $\nabla \cdot \boldsymbol{q}_{M}$ and $\nabla \cdot \boldsymbol{q}_{m}$ from equations (37) and (38). Inserting equations (46) and (47) into equation (45) and collecting terms, we obtain

$$\rho \dot{e} = \boldsymbol{\sigma}' : \boldsymbol{d}^e + \boldsymbol{\sigma}'' : \boldsymbol{d}^p + \theta_M \dot{p}_M + \theta_m \dot{p}_m + \boldsymbol{\chi}_M \cdot \tilde{\boldsymbol{v}}_M + \boldsymbol{\chi}_m \cdot \tilde{\boldsymbol{v}}_m + \zeta \dot{\psi} + \sum_{M,m} \left(\frac{1}{2} c_\alpha \boldsymbol{v}_\alpha \cdot \boldsymbol{v}_\alpha - \frac{c_\alpha p_\alpha}{\rho_\alpha} \right) , \quad (48)$$

where $\psi := \psi^M$ and $(\dot{\cdot}) = d(\cdot)/dt$. Each term on the right hand side represents an energy-conjugate pair related by a constitutive law. As in classic poromechanics with one porosity scale [117], two effective stress tensors emerge in this expression:

$$\boldsymbol{\sigma}' = \boldsymbol{\sigma} + (\psi^M p_M + \psi^m p_m) \boldsymbol{b} = \boldsymbol{\sigma} + \overline{p} \boldsymbol{b}, \tag{49}$$

which is conjugate to the elastic component of the rate of deformation tensor \boldsymbol{d}^e , and

$$\boldsymbol{\sigma}'' = \boldsymbol{\sigma} + (\psi^M p_M + \psi^m p_m) \mathbf{1} = \boldsymbol{\sigma} + \overline{p} \mathbf{1}, \qquad (50)$$

which is conjugate to the plastic component d^p . The remaining terms in the expression are given as follows,

$$\theta_M = \frac{p_M \phi^M}{K_M} + \frac{\psi^M \overline{p} \beta}{K_s},\tag{51a}$$

$$\theta_m = \frac{p_m \phi^m}{K_m} + \frac{\psi^m \overline{p} \beta}{K_s},\tag{51b}$$

$$\chi_M = \left(\nabla \phi^M + \frac{\phi^M}{K_M} \nabla p_M\right) p_M, \tag{51c}$$

$$\chi_m = \left(\nabla \phi^m + \frac{\phi^m}{K_m} \nabla p_m\right) p_m, \tag{51d}$$

$$\zeta = \left(\phi + \frac{\beta \overline{p}}{K_s}\right)(p_M - p_m). \tag{51e}$$

Note that both effective stress tensors can be constructed as linear combinations of the total Cauchy stress tensor σ and the mean pore pressure \overline{p} . For σ' , \overline{p} is scaled with the Biot tensor \boldsymbol{b} , while for σ'' , \overline{p} is scaled with the Kronecker delta tensor [97, 98]. The two effective stress tensors defined in equations (49) and (50) reduce to those derived for single porosity media when $p_M = p_m \equiv p$ [117]. Furthermore, for isotropic media the Biot tensor \boldsymbol{b} reduces to the form

$$\boldsymbol{b} = \left(1 - \frac{K}{K_s}\right) \boldsymbol{1} \,, \tag{52}$$

where K is the elastic bulk modulus of the solid matrix. This last expression is identical to the one developed by Borja and Koliji [17].

Finally, we recall the assumed form of the effective stress tensor σ' in equation (18). Comparing this form with equation (49), we readily conclude that

$$\alpha = b = 1 - \frac{1 : \mathbb{C}^e}{3K_s}. \tag{53}$$

Furthermore,

$$\beta = \frac{1}{3}\mathbf{1} : \boldsymbol{b} - \phi = \overline{b} - \phi, \tag{54}$$

where \bar{b} is the equivalent Biot coefficient, which reduces to the conventional Biot coefficient $(1 - K/K_s)$ for isotropic materials.

Remark 1. An alternative derivation would be to assume that in lieu of equation (18), we begin with the more general form

$$\boldsymbol{\sigma} = \boldsymbol{\sigma}' - p_M \boldsymbol{\alpha}_M - p_m \boldsymbol{\alpha}_m \,. \tag{55}$$

It can be shown that following the same derivation also yields equation (49), i.e., $\alpha_M = \psi^M \mathbf{b}$ and $\alpha_m = \psi^m \mathbf{b}$. This implies that the mean pore pressure \overline{p} must be used in defining the effective stresses.

2.5 Reduced dissipation inequality

Consider a free energy density function Ψ that is quadratic in the elastic strains. Specializing to infinitesimal deformation, we can write the Clausius-Duhem inequality in the form

$$\mathcal{D} = \rho \dot{e} - \dot{\Psi}$$

$$= \boldsymbol{\sigma}' : \dot{\boldsymbol{\epsilon}}^e + \boldsymbol{\sigma}'' : \dot{\boldsymbol{\epsilon}}^p + \theta_M \dot{p}_M + \theta_m \dot{p}_m + \boldsymbol{\chi}_M \cdot \widetilde{\boldsymbol{v}}_M$$

$$+ \boldsymbol{\chi}_m \cdot \widetilde{\boldsymbol{v}}_m + \zeta \dot{\psi} + \sum_{M,m} \left(\frac{1}{2} c_{\alpha} \boldsymbol{v}_{\alpha} \cdot \boldsymbol{v}_{\alpha} - \frac{c_{\alpha} p_{\alpha}}{\rho_{\alpha}} \right) - \dot{\Psi} \ge 0, \qquad (56)$$

where the infinitesimal strain rate tensor $\dot{\epsilon}$ replaces the rate of deformation tensor d. The Coleman relations [71] yield, among others, the elastic constitutive equation

$$\sigma' = \frac{\partial \Psi}{\partial \epsilon^e} = \mathbb{C}^e : \epsilon^e, \tag{57}$$

which suggests that the elastic response is determined by the effective stress tensor σ' .

The reduced dissipation inequality consists of two parts,

$$\mathcal{D} = \mathcal{D}^p + \mathcal{D}^{\text{trans}} > 0, \tag{58}$$

where \mathcal{D}^p is dissipation triggered by mechanical plastic deformation and $\mathcal{D}^{\text{trans}}$ is dissipation generated by fluid mass transfer across the two pore scales. Among the terms in \mathcal{D}^p is the plastic dissipation produced by the effective stress σ'' ,

$$\boldsymbol{\sigma}'': \dot{\boldsymbol{\epsilon}}^p \ge 0. \tag{59}$$

If we define a yield function $f(\sigma'', p_c) \leq 0$, where p_c is some plastic internal variable that reflects the hardening/softening response of the material [32, 40, 111, 112], and if we impose the associative flow rule [19]

$$\dot{\boldsymbol{\epsilon}}^p = \dot{\lambda} \frac{\partial f}{\partial \boldsymbol{\sigma}''}, \tag{60}$$

where $\dot{\lambda} \geq 0$ is a nonnegative plastic multiplier, then non-negativity of plastic dissipation requires that

$$\sigma'': \frac{\partial f}{\partial \sigma''} \ge 0, \tag{61}$$

which is met by a convex yield function f in the stress space σ'' [19].

As for dissipation resulting from fluid mass transfer, the condition takes the form

$$\mathcal{D}^{\text{trans}} = \sum_{M,m} \left(\frac{1}{2} c_{\alpha} \boldsymbol{v}_{\alpha} \cdot \boldsymbol{v}_{\alpha} - \frac{c_{\alpha} p_{\alpha}}{\rho_{\alpha}} \right) \ge 0.$$
 (62)

Non-negativity of this function must be ensured when developing constitutive models for the mass transfer term $c_M = -c_m$.

Remark 2. Due to the small-strain assumption, the plasticity model employed in this work and described briefly in the next section does not include changes in the internal structure of the material in the form of the evolution of pore fractions ψ^M and ψ^m . The reader is referred to Borja and Choo [21] on how to incorporate this feature into the modified Cam-Clay theory for double-porosity media.

3 Constitutive equations

The developments of the previous section suggest that the solid deformation component of the double-porosity theory is essentially the same as the one developed for classic single-porosity theory except that one must now use the mean pore pressure \bar{p} in lieu of the single pore pressure variable p [117]. In what follows, we briefly summarize the main features of the solid deformation model and simply refer the readers to Zhao and Borja [117] for further details.

3.1 Solid deformation

We again use the concept of alternative strain $\tilde{\epsilon}$ introduced in [117] to eliminate one of the two effective stresses. In the present case, we eliminate σ' and write the elastic constitutive equation for σ'' as

$$\boldsymbol{\sigma}'' = \mathbb{C}^e : \widetilde{\boldsymbol{\epsilon}}^e, \tag{63}$$

where

$$\widetilde{\boldsymbol{\epsilon}}^e = {\boldsymbol{\epsilon}}^e + \mathbb{C}^{e-1} : (\mathbf{1} - {\boldsymbol{b}})\overline{p}$$
 (64)

is an alternative elastic strain tensor. Furthermore, we set an alternative plastic strain tensor as

$$\widetilde{\boldsymbol{\epsilon}}^p = {\boldsymbol{\epsilon}}^p \qquad \Longrightarrow \qquad \dot{\widetilde{\boldsymbol{\epsilon}}}^p = \dot{\boldsymbol{\epsilon}}^p = \dot{\lambda} \frac{\partial f}{\partial {\boldsymbol{\sigma}}''} \,.$$
 (65)

The alternative total strain tensor is then the sum of the elastic and plastic parts,

$$\widetilde{\epsilon} = \widetilde{\epsilon}^e + \widetilde{\epsilon}^p \,. \tag{66}$$

A transversely isotropic material is characterized by a microstructure tensor given by

$$m = n \otimes n . \tag{67}$$

This tensor can be used to define the five-constant elastic tangent operator

$$\mathbb{C}^{e} = \lambda \mathbf{1} \otimes \mathbf{1} + 2\mu_{T} \mathbb{I} + a(\mathbf{1} \otimes \mathbf{m} + \mathbf{m} \otimes \mathbf{1}) + b\mathbf{m} \otimes \mathbf{m} + (\mu_{L} - \mu_{T})(\mathbf{1} \oplus \mathbf{m} + \mathbf{m} \oplus \mathbf{1} + \mathbf{1} \ominus \mathbf{m} + \mathbf{m} \ominus \mathbf{1}),$$
(68)

where λ , μ_L , μ_T , a, and b are the aforementioned constants. The Biot tensor \boldsymbol{b} for a transversely isotropic material can be written in the form

$$\boldsymbol{b} = b_{\perp} \boldsymbol{m} + b_{\parallel} (\boldsymbol{1} - \boldsymbol{m}), \tag{69}$$

where

$$b_{\perp} = 1 - \frac{3\lambda + 4a + b + 4\mu_L - 2\mu_T}{3K_s}$$

$$b_{\parallel} = 1 - \frac{3\lambda + 2\mu_T + a}{3K_s}$$
(70a)

$$b_{\parallel} = 1 - \frac{3\lambda + 2\mu_T + a}{3K_s} \tag{70b}$$

are the Biot coefficients along the axis of anisotropy and plane of isotropy, respectively, see [36, 88].

In the context of anisotropic elasto-plasticity, we construct an anisotropic yield surface from the modified Cam-Clay model [22, 90, 115, 116], first by rotating the effective Cauchy stress tensor σ'' to a fictitious stress space defined by

$$\sigma^* = \mathbb{P} : \sigma'', \tag{71}$$

and then writing the yield function as

$$f(\boldsymbol{\sigma}^*, p_c) = \frac{q^{*2}}{M^2} + p^*(p^* - p_c) \le 0,$$
 (72)

where $p^* = \frac{1}{3}\mathbf{1} : \boldsymbol{\sigma}^*$, $q^* = \sqrt{\frac{3}{2}} \|\mathbf{s}^*\|$, and $\mathbf{s}^* = \boldsymbol{\sigma} - p^*\mathbf{1}$. The idea behind the rotation operation is to write the yield function in terms of the rotated tensor $\boldsymbol{\sigma}^*$ in a two-invariant isotropic form. To complete the plasticity model, we write the hardening law as

$$p_c = p_{c0} \exp\left(-\frac{\epsilon_v^p}{\lambda^p}\right),\tag{73}$$

where ϵ_{v}^{p} is the plastic volumetric strain.

The rank-four rotation tensor is given by the expression

$$\mathbb{P} = c_1 \mathbb{I} + \frac{c_2}{2} (\boldsymbol{m} \oplus \boldsymbol{m} + \boldsymbol{m} \ominus \boldsymbol{m}) + \frac{c_3}{4} (\mathbf{1} \oplus \boldsymbol{m} + \boldsymbol{m} \oplus \mathbf{1} + \mathbf{1} \ominus \boldsymbol{m} + \boldsymbol{m} \ominus \mathbf{1}),$$
 (74)

where c_1 , c_2 , and c_3 are the anisotropy parameters. We note that the rotation operator \mathbb{P} includes the microstructure tensor m defining the orientation of the plane of isotropy.

To summarize, the plasticity model includes 3 parameters of the modified Cam-clay theory, namely, M, λ^p , and p_{c0} ; and the anisotropy parameters c_1 , c_2 , and c_3 .

3.2 Fluid flow and mass transfer

Darcy's law is adopted to model fluid flow in both macropores and micropores,

$$\boldsymbol{q}_{\alpha} = \phi^{\alpha} \widetilde{\boldsymbol{v}}_{\alpha} = -\frac{\boldsymbol{\kappa}_{\alpha}}{\mu_{f}} (\nabla p_{\alpha} - \rho_{\alpha} \boldsymbol{g}), \qquad \alpha = M, m,$$
 (75)

where q_{α} is the Darcy velocity and κ_{α} is the intrinsic permeability in pore scale α , and μ_f is the dynamic viscosity of fluid. Considering preferential flow along the plane of isotropy in the macropores, the intrinsic permeability tensor in the macropores may be written in terms of the components κ_{\perp} along the axis of anisotropy and κ_{\parallel} on the plane of isotropy as [113]

$$\boldsymbol{\kappa}_M = \kappa_{\perp} \boldsymbol{m} + \kappa_{\parallel} (1 - \boldsymbol{m}). \tag{76}$$

We assume that the intrinsic permeability in the micropores is isotropic and write

$$\kappa_m = \kappa_m \mathbf{1}.\tag{77}$$

As for the mass transfer terms c_m and c_M , a first-order mass transfer equation is proposed as follows [113]

$$\frac{c_M}{\rho_M} = \overline{k} \frac{\overline{\alpha}}{\mu_f} (p_m - p_M), \qquad \frac{c_m}{\rho_m} = \overline{k} \frac{\overline{\alpha}}{\mu_f} (p_M - p_m), \qquad \overline{\alpha} = \frac{\overline{\beta}}{\overline{a}^2} \overline{\gamma}, \tag{78}$$

where \overline{k} is the interface permeability, \overline{a} is the characteristic length of the macropores spacing, $\overline{\beta}$ is a dimensionless coefficient that accounts for the solid matrix geometry, and $\overline{\gamma}$ is a dimensionless scaling coefficient suggested to be 0.4 to fit experimental results [48]. Inserting the foregoing constitutive equations into the dissipation inequality yields

$$\mathcal{D}^{\text{trans}} = \overline{k} \frac{\overline{\alpha}}{\mu_f} (p_M - p_m)^2 + \frac{1}{2} c_M \left(\boldsymbol{v}_M \cdot \boldsymbol{v}_M - \boldsymbol{v}_m \cdot \boldsymbol{v}_m \right) \ge 0.$$
 (79)

The first term on the right hand side is always non-negative; the second term is non-negative if $c_M \geq 0$ and $\|\boldsymbol{v}_M\| \geq \|\boldsymbol{v}_m\|$, or $c_M \leq 0$ and $\|\boldsymbol{v}_M\| \leq \|\boldsymbol{v}_m\|$. This implies that fluid must drain into the pore scale where the fluid is flowing faster. Given that fluid generally flows faster in the macropores because of the larger pore sizes, a non-negative dissipation requires that fluid in the micropores should drain into the macropores, see [21].

4 Mixed finite element formulation

We employ the standard Galerkin mixed finite element formulation in which the main unknown variables are the solid displacement u and fluid pressures p_M and p_m . Equal-order (linear) interpolation is adopted for the displacement and pressure fields to reduce the size of the matrix problem, and a numerical stabilization is implemented to address the inf-sup condition in the incompressible and nearly incompressible regimes.

4.1 Strong Form

Consider a closed domain $\overline{\mathcal{B}} = \mathcal{B} \cup \partial \mathcal{B}$. We decompose the boundary $\partial \mathcal{B}$ into non-overlaping essential and natural boundaries $\partial \mathcal{B}_u$ and $\partial \mathcal{B}_t$, respectively, where solid displacement and surface tractions are prescribed; $\partial \mathcal{B}_{p_M}$ and $\partial \mathcal{B}_{q_M}$, where fluid pressure and flux through the macropores are prescribed; and $\partial \mathcal{B}_{p_m}$ and $\partial \mathcal{B}_{q_m}$, where fluid pressure and flux through the micropores are specified. The following relations must hold on the boundaries:

Anisotropic elastoplastic response of double-porosity media

$$\overline{\partial \mathcal{B}_u \cup \partial \mathcal{B}_t} = \overline{\partial \mathcal{B}_{p_M} \cup \partial \mathcal{B}_{q_M}} = \overline{\partial \mathcal{B}_{p_m} \cup \partial \mathcal{B}_{q_m}} = \partial \mathcal{B}, \tag{80a}$$

19

$$\partial \mathcal{B}_u \cap \partial \mathcal{B}_t = \partial \mathcal{B}_{p_M} \cap \partial \mathcal{B}_{q_M} = \partial \mathcal{B}_{p_m} \cap \partial \mathcal{B}_{q_m} = \varnothing,$$
 (80b)

where the overline denotes a closure.

The strong form of the initial boundary-value problem is stated as follows. Find u, p_M , and p_m such that the following conservation laws are satisfied:

Balance of linear momentum for the mixture:

$$\nabla \cdot (\boldsymbol{\sigma}'' - \overline{p}\mathbf{1}) + \rho \boldsymbol{g} = \overline{\boldsymbol{c}} \quad \text{in} \quad \mathcal{B}.$$
 (81)

Balance of fluid mass in the macropores:

$$\psi^{M} \boldsymbol{b} : \dot{\boldsymbol{\epsilon}}^{e} + \psi^{M} \boldsymbol{1} : \dot{\boldsymbol{\epsilon}}^{p} + \nabla \cdot \boldsymbol{q}_{M} + \frac{1}{K_{M}} \nabla p_{M} \cdot \boldsymbol{q}_{M} + S_{Mm} \dot{p}_{M} + S_{Mm} \dot{p}_{m} = \frac{c_{M}}{\rho_{M}} \quad \text{in} \quad \mathcal{B} . \quad (82)$$

Balance of fluid mass in the micropores:

$$\psi^{m} \mathbf{b} : \dot{\mathbf{e}}^{e} + \psi^{m} \mathbf{1} : \dot{\mathbf{e}}^{p} + \nabla \cdot \mathbf{q}_{m} + \frac{1}{K_{m}} \nabla p_{m} \cdot \mathbf{q}_{m} + S_{mm} \dot{p}_{m} + S_{mm} \dot{p}_{m} = \frac{c_{m}}{\rho_{m}} \quad \text{in} \quad \mathcal{B} . \tag{83}$$

In addition, the following boundary conditions must be satisfied:

Solid deformation:

Fluid flow in the macropores:

$$p_M = \hat{p}_M \text{ on } \partial \mathcal{B}_{p_M} \\
- \mathbf{n} \cdot \mathbf{q}_M = \hat{q}_M \text{ on } \partial \mathcal{B}_{q_M}$$
(85)

Fluid flow in the micropores:

$$p_m = \hat{p}_m \text{ on } \partial \mathcal{B}_{p_m} \\
 -\mathbf{n} \cdot \mathbf{q}_m = \hat{q}_m \text{ on } \partial \mathcal{B}_{q_m}$$
(86)

We also need the following initial conditions on the unknown variables:

$$\begin{aligned} u(\boldsymbol{x}, t = 0) &= u_0(\boldsymbol{x}) \\ p_M(\boldsymbol{x}, t = 0) &= p_{M0}(\boldsymbol{x}) \\ p_m(\boldsymbol{x}, t = 0) &= p_{m0}(\boldsymbol{x}) \end{aligned}$$
 (87)

for all $x \in \overline{\mathcal{B}}$.

4.2 Weak Form

We first define sets of trial functions

$$\mathcal{S}_{u} = \{ \boldsymbol{u} | \boldsymbol{u} \in H^{1}, \ \boldsymbol{u} = \hat{\boldsymbol{u}} \text{ on } \partial \mathcal{B}_{u} \}
\mathcal{S}_{p_{M}} = \{ p_{M} | p_{M} \in H^{1}, \ p_{M} = \hat{p}_{M} \text{ on } \partial \mathcal{B}_{p_{M}} \}
\mathcal{S}_{p_{m}} = \{ p_{m} | p_{m} \in H^{1}, \ p_{m} = \hat{p}_{m} \text{ on } \partial \mathcal{B}_{p_{m}} \}$$
(88)

and sets of weighting functions

$$\mathcal{V}_{u} = \{ \boldsymbol{\eta} | \boldsymbol{\eta} \in H^{1}, \ \boldsymbol{\eta} = \mathbf{0} \text{ on } \partial \mathcal{B}_{u} \}
\mathcal{V}_{p_{M}} = \{ \varphi_{M} | \varphi_{M} \in H^{1}, \ \varphi_{M} = 0 \text{ on } \partial \mathcal{B}_{p_{M}} \}
\mathcal{V}_{p_{m}} = \{ \varphi_{m} | \varphi_{m} \in H^{1}, \ \varphi_{m} = 0 \text{ on } \partial \mathcal{B}_{p_{m}} \}$$
(89)

For the weak form, we want to find $\{\boldsymbol{u}, p_M, p_m\} \in \mathcal{S}_u \times \mathcal{S}_{p_M} \times \mathcal{S}_{p_m}$ such that for all $\{\boldsymbol{\eta}, \varphi_M, \varphi_m\} \in \mathcal{V}_u \times \mathcal{V}_{p_M} \times \mathcal{V}_{p_m}$ the following variational equations are satisfied:

Balance of linear momentum:

$$\int_{\mathcal{B}} \nabla^{s} \boldsymbol{\eta} : (\boldsymbol{\sigma}'' - \overline{p} \mathbf{1}) \, dV = \int_{\mathcal{B}} \boldsymbol{\eta} \cdot (\rho \boldsymbol{g} - \overline{\boldsymbol{c}}) \, dV + \int_{\partial \mathcal{B}_{s}} \boldsymbol{\eta} \cdot \hat{\boldsymbol{t}} \, dA, \qquad (90)$$

where ∇^s is the symmetric gradient operator.

Fluid flow in the macropores:

$$\int_{\mathcal{B}} \varphi_{M} \left(\psi^{M} \boldsymbol{b} : \dot{\boldsymbol{\epsilon}}^{e} + \psi^{M} \boldsymbol{1} : \dot{\boldsymbol{\epsilon}}^{p} + \frac{1}{K_{M}} \nabla p_{M} \cdot \boldsymbol{q}_{M} + S_{MM} \dot{p}_{M} + S_{Mm} \dot{p}_{m} \right) dV
- \int_{\mathcal{B}} \varphi_{M} \left(\frac{c_{M}}{\rho_{M}} \right) dV - \int_{\mathcal{B}} \nabla \varphi_{M} \cdot \boldsymbol{q}_{M} = \int_{\partial \mathcal{B}_{q_{M}}} \varphi_{M} \hat{q}_{M} dA . \tag{91}$$

Fluid flow in the micropores:

$$\int_{\mathcal{B}} \varphi_{m} \Big(\psi^{m} \boldsymbol{b} : \dot{\boldsymbol{\epsilon}}^{e} + \psi^{m} \boldsymbol{1} : \dot{\boldsymbol{\epsilon}}^{p} + \frac{1}{K_{m}} \nabla p_{m} \cdot \boldsymbol{q}_{m} + S_{mM} \dot{p}_{M} + S_{mm} \dot{p}_{m} \Big) dV
- \int_{\mathcal{B}} \varphi_{m} \Big(\frac{c_{m}}{\rho_{m}} \Big) dV - \int_{\mathcal{B}} \nabla \varphi_{m} \cdot \boldsymbol{q}_{m} dV = \int_{\partial \mathcal{B}_{q_{m}}} \varphi_{m} \hat{q}_{m} dA. \quad (92)$$

4.3 Matrix Form

We next replace the trial and weighting functions with their approximations $\boldsymbol{u}^h, p_M^h, p_m^h, \boldsymbol{\eta}^h, \varphi_M^h$ and φ_m^h . Then, we integrate in time using the first order, unconditionally stable backward difference integration scheme, and in space using standard shape functions, given as

where N_{\square} denotes the shape function matrix that interpolates the variable \square . Nodal values of the unknown variables are assembled in the vectors of unknowns d, p_M, p_m ; the hat symbols pertain to contributions from the essential boundary conditions. Gradients of the unknown variables are interpolated according to the following equations

$$\nabla^{s} \boldsymbol{u}^{h} = \boldsymbol{B} \boldsymbol{d} + \hat{\boldsymbol{B}} \hat{\boldsymbol{d}}
\nabla p_{M}^{h} = \boldsymbol{E} \boldsymbol{p}_{M} + \hat{\boldsymbol{E}} \hat{\boldsymbol{p}}_{M}
\nabla p_{m}^{h} = \boldsymbol{E} \boldsymbol{p}_{m} + \hat{\boldsymbol{E}} \hat{\boldsymbol{p}}_{m}$$
(94)

Equal-order interpolations are employed on all the unknown variables (bilinear for 2D).

Next, we assemble the global matrix equation in residual form for subsequent solution by Newton iteration. For balance of linear momentum, the residual equation is given by

$$\mathcal{R}_{u} = \int_{\mathcal{B}} \boldsymbol{B}^{\mathsf{T}} (\boldsymbol{\sigma}'' - \overline{p}^{h} \mathbf{1}) \, dV - \int_{\mathcal{B}} \boldsymbol{N}_{u}^{\mathsf{T}} (\rho \boldsymbol{g} - \overline{\boldsymbol{c}}) \, dV - \int_{\partial \mathcal{B}_{t}} \boldsymbol{N}_{u}^{\mathsf{T}} \hat{\boldsymbol{t}} \, dA.$$
 (95)

For fluid flow in the macropores, we have

$$\mathcal{R}_{p_{M}} = \int_{\mathcal{B}} \mathbf{N}_{p}^{\mathsf{T}} \left[\psi^{M} \mathbf{1} : (\boldsymbol{\epsilon} - \boldsymbol{\epsilon}_{n}) + \psi^{M} (\boldsymbol{b} - \mathbf{1}) : (\boldsymbol{\epsilon}^{e} - \boldsymbol{\epsilon}_{n}^{e}) \right] dV
+ \int_{\mathcal{B}} \mathbf{N}_{p}^{\mathsf{T}} \left[S_{MM} (p_{M}^{h} - p_{M,n}^{h}) + S_{Mm} (p_{m}^{h} - p_{m,n}^{h}) - \frac{\Delta t c_{M}}{\rho_{M}} \right] dV
+ \int_{\mathcal{B}} \mathbf{N}_{p}^{\mathsf{T}} \left(\frac{\Delta t}{K_{M}} \nabla p_{M}^{h} \cdot \boldsymbol{q}_{M} \right) dV - \int_{\mathcal{B}} \Delta t \boldsymbol{E}^{\mathsf{T}} \boldsymbol{q}_{M} dV
- \int_{\partial \mathcal{B}_{MM}} \Delta t \boldsymbol{N}_{p}^{\mathsf{T}} \hat{q}_{M} dA .$$
(96)

And for fluid flow in the micropores, the residual equation is given by

$$\mathcal{R}_{p_{m}} = \int_{\mathcal{B}} \mathbf{N}_{p}^{\mathsf{T}} [\psi^{m} \mathbf{1} : (\boldsymbol{\epsilon} - \boldsymbol{\epsilon}_{n}) + \psi^{m} (\boldsymbol{b} - \mathbf{1}) : (\boldsymbol{\epsilon}^{e} - \boldsymbol{\epsilon}_{n}^{e})] dV
+ \int_{\mathcal{B}} \mathbf{N}_{p}^{\mathsf{T}} \Big[S_{mM} (p_{M}^{h} - p_{M,n}^{h}) + S_{mm} (p_{m}^{h} - p_{m,n}^{h}) - \frac{\Delta t c_{m}}{\rho_{m}} \Big] dV
+ \int_{\mathcal{B}} \mathbf{N}_{p}^{\mathsf{T}} \Big(\frac{\Delta t}{K_{m}} \nabla p_{m}^{h} \cdot \boldsymbol{q}_{m} \Big) dV - \int_{\mathcal{B}} \Delta t \boldsymbol{E}^{\mathsf{T}} \boldsymbol{q}_{m} dV
- \int_{\partial \mathcal{B}_{q_{m}}} \Delta t \boldsymbol{N}_{p}^{\mathsf{T}} \hat{q}_{m} dA .$$
(97)

The final step is to solve the system of nonlinear equations using Newton's method. The solution requires construction of an algorithmic tangent operator K for use in the linearized equation

$$\begin{bmatrix}
K_{11} K_{12} K_{13} \\
K_{21} K_{22} K_{23} \\
K_{31} K_{32} K_{33}
\end{bmatrix}
\begin{cases}
\delta d \\
\delta p_M \\
\delta p_m
\end{cases} = -
\begin{cases}
\mathcal{R}_u \\
\mathcal{R}_{p_M} \\
\mathcal{R}_{p_m}
\end{cases},$$
(98)

where $(\delta \boldsymbol{d}, \delta \boldsymbol{p}_M, \delta \boldsymbol{p}_m)$ are the search directions [19]. Analytical expressions for the algorithmic tangent operator are reported in Appendix A.

4.4 Stabilized mixed elements

In this work, we adopt an equal-order (bilinear in 2D) interpolation for both displacement and pressure fields. A typical numerical issue associated with equal-order interpolation in mixed finite element analysis is the instability associated with non-satisfaction of the inf-sup condition [95, 104], which arises not only in single-porosity formulations [27, 106] but also in double-porosity problems [31, 35] in the incompressible and nearly incompressible regimes.

To address this issue, we employ the stabilization scheme proposed by Choo and Borja [31], where a stabilization term is constructed based on the polynomial pressure projection method proposed by Bochev et al. [11]. This stabilization term is then scaled with a stabilization parameter c, split by the fractions of porosity and associated with the residual equations of the pressure fields. To account for the anisotropic and plastic response of the solid skeleton, a different stabilization parameter similar to the one proposed by White and Borja [106] is used in this framework, defined as $c = \tau/2G$. Here, G is identified as the lower value of the elastic shear moduli μ_L and μ_T . Since we adopt the elastic moduli rather than the elastoplastic tangent moduli in quantifying G to avoid additional nonlinearity to the overall system, a tunable parameter τ is introduced to refine the level of stabilization.

5 Numerical examples

5.1 1D consolidation of Opalinus clay shale

Shale is an energy-bearing matrix in unconventional reservoirs. As a tight and ductile rock, it can serve as a seal for CO₂ geological sequestration [51, 52, 74, 119], or a host material for nuclear waste disposal [15, 28, 30, 68, 84, 107]. With a laminated microstructure developed from sedimentation or diagenesis, shale exhibits an anisotropic mechanical behavior that is more accurately characterized as transversely isotropic [3, 6, 14, 38, 39, 54, 57, 73, 78, 80, 85, 89, 94]. As a salient character of transversely isotropic rocks, the impact of bedding plane is typically reflected in the constitutive description of the solid matrix [25, 41, 65, 66].

This section reproduces the hydromechanical response of Opalinus clay shale from Switzerland during one-dimensional consolidation test. This shale is an overconsolidated sedimentary rock containing partially-bonded laminated microstructure through diagenetic processes [45]. It has been considered to serve as the host material for the construction of a nuclear waste repository in Switzerland, and thus, in recent years, the mechanical response, failure behaviors, and hydromechanical properties of this shale have been well investigated [37, 45–47, 76]. The vastly and completely reported experimental data on Opalinus clay shale in the literature enabled us to calibrate the model and conduct numerical simulations over the same batch of specimens.

The specimens of Opalinus clay shale we investigated were retrieved from the Mont Terri Underground Rock Laboratory in northwestern Switzerland located at a depth of approximately 300 m, and the maximum depth during its burial history was around 1200 m. Mineral compositions of the specimens are very similar, the majority of which include clay (66%–67%), quartz (9%–13%), and calcite (13%–17%) [46, 47]. As a matter of terminology for this specific material where the pore scale is smaller than that of, say, soils, the term 'micropores' pertain to the nanoscale pores of kerogen and clay matrix, whereas 'macropores' pertain to the rock's micro-fractures [113].

Favero et al. [46] conducted drained triaxial compression tests on Opalinus clay shale with samples cored either perpendicular to the bedding plane $(\theta = 0^{\circ})$ or parallel to the bedding plane $(\theta = 90^{\circ})$. Here, we calibrated the elasticity and plasticity parameters for solid deformation with the reported experimental data for the case where the confining pressure was 5 MPa, as shown in Table 1. A comparison between simulation results and experimental data of stress and volumetric strain development during the triaxial compression test is shown in Figure 1.

Ferrari et al. [47] conducted one-dimensional consolidation tests on Opalinus clay shale cored perpendicular to the bedding plane ($\theta=0^{\circ}$). The specimens used in the experiments were 12 mm thick and drained on both the top and bottom surfaces. Figure 2 illustrates the setup of the test. The consolidation process was conducted with different loads ω . The experimental apparatus was unable to apply the load instantaneously, so each load increment was applied within two stages where each stage was applied at a constant rate. Sixty percent of the load increment was applied within 60 seconds, the rest within the next 160 seconds as illustrated in Figure 3.

We used the parameters already calibrated for solid deformation while calibrating the parameters for fluid flow. For the consolidation problem, we used a lower initial preconsolidation stress $p_{c0} = -4$ MPa for purposes of achieving a better fit with experimental results. Specimens used in the triaxial and consolidation tests had some uncertainties with respect to stress history, and so we had to assume an initial preconsolidation stress. The bulk modulus of solid K_s was selected according to the literature [47], and the corresponding effective Biot coefficient was estimated to be around $\bar{b} = 0.88$. We assumed that fluid could not flow within the micropores ($\kappa_m = 0$), but could drain into

the macropores. The load increments were applied in sequence, and for each load increment the simulation continued until the sample was fully drained. The solution at the fully drained condition at the current load level was then taken as the initial condition for simulating the next load increment.

Figure 4 shows the evolutions of settlement and pore pressure during the 1D consolidation test. Different load increments were considered covering loading, unloading, and reloading processes. The figure shows that even with a single set of calibrated parameters, the model can capture the overall trend of settlement evolution during different phases including load application, primary consolidation, and secondary consolidation under different load increments. Figure 4(f) reveals the evolution of average pore pressure \bar{p} evaluated in the middle of the domain for the reloading process, reflecting a typical pore pressure dissipation process for double porosity media. The initial drop of mean pore pressure \bar{p} corresponds to the primary consolidation process where drainage of fluid in the macropores governs such a response. The drainage process takes longer to complete as the fluid in the micropores drains into the macropores, leading to secondary consolidation.

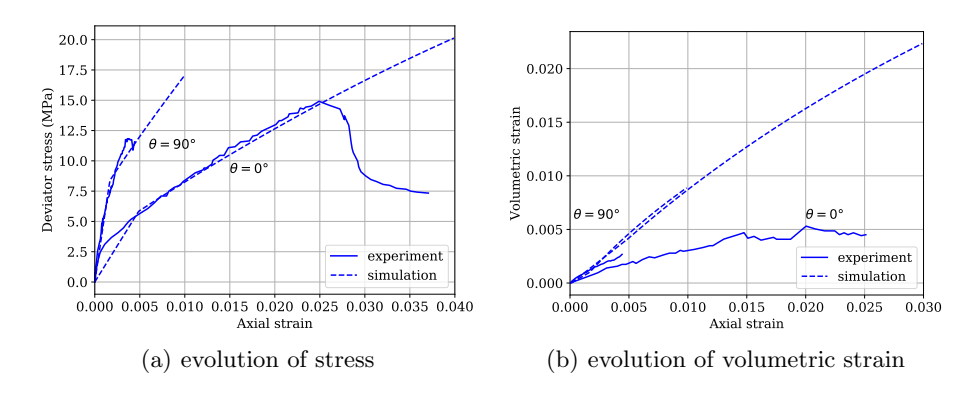


Fig. 1. Model calibration for Opalinus clay shale.

5.2 Plane strain consolidation under a strip load

This 2D example demonstrates the performance of the proposed stabilization scheme as well as investigates the influence of stress history, mass transfer, and different pore systems (single versus double porosity) on the system response. The problem consists of a rectangular domain with dimensions 20 m \times 10 m and boundary conditions shown in Figure 5. The plane of isotropy (or bedding plane) is oriented at $\theta=45^{\circ}$ with the horizontal. Parameters adopted in the simulations are summarized in Table 2. For mechanical deformation, the parameters were originally calibrated from the properties of Tournemire

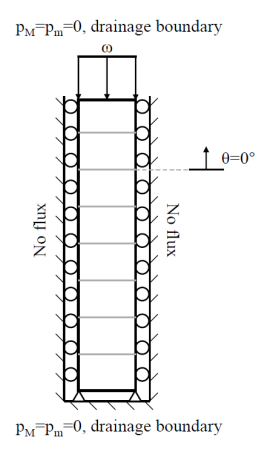


Fig. 2. Illustration of the one-dimensional consolidation problem.

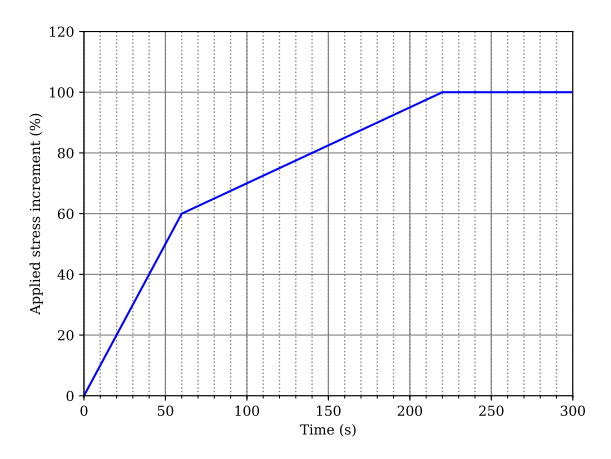


Fig. 3. Schematic diagram of the two-staged stress increment application

shale [115]. The bulk modulus K_s was chosen such that $\bar{b} = 0.8$. Gravity is ignored in the simulation by setting g = 0.

Both normally consolidated (NC) domain with $p_{c0} = -1$ MPa and over-consolidated (OC) domain with $p_{c0} = -2$ MPa were simulated. The initial condition was established by applying an overburden pressure of $p_0 = 1$ MPa under a fully drained condition. Then, a strip load of $\omega = 1$ MPa covering a width of 2 m was applied in 10 s, a period short enough that fluid flow was nearly suppressed to set up a nearly undrained condition in the two pore scales.

We first present the undrained response with and without numerical stabilization. In the undrained limit, the distributions of p_M and p_m are identical; thus, we only show the results for the micropore pressure p_m . Figure 6 shows

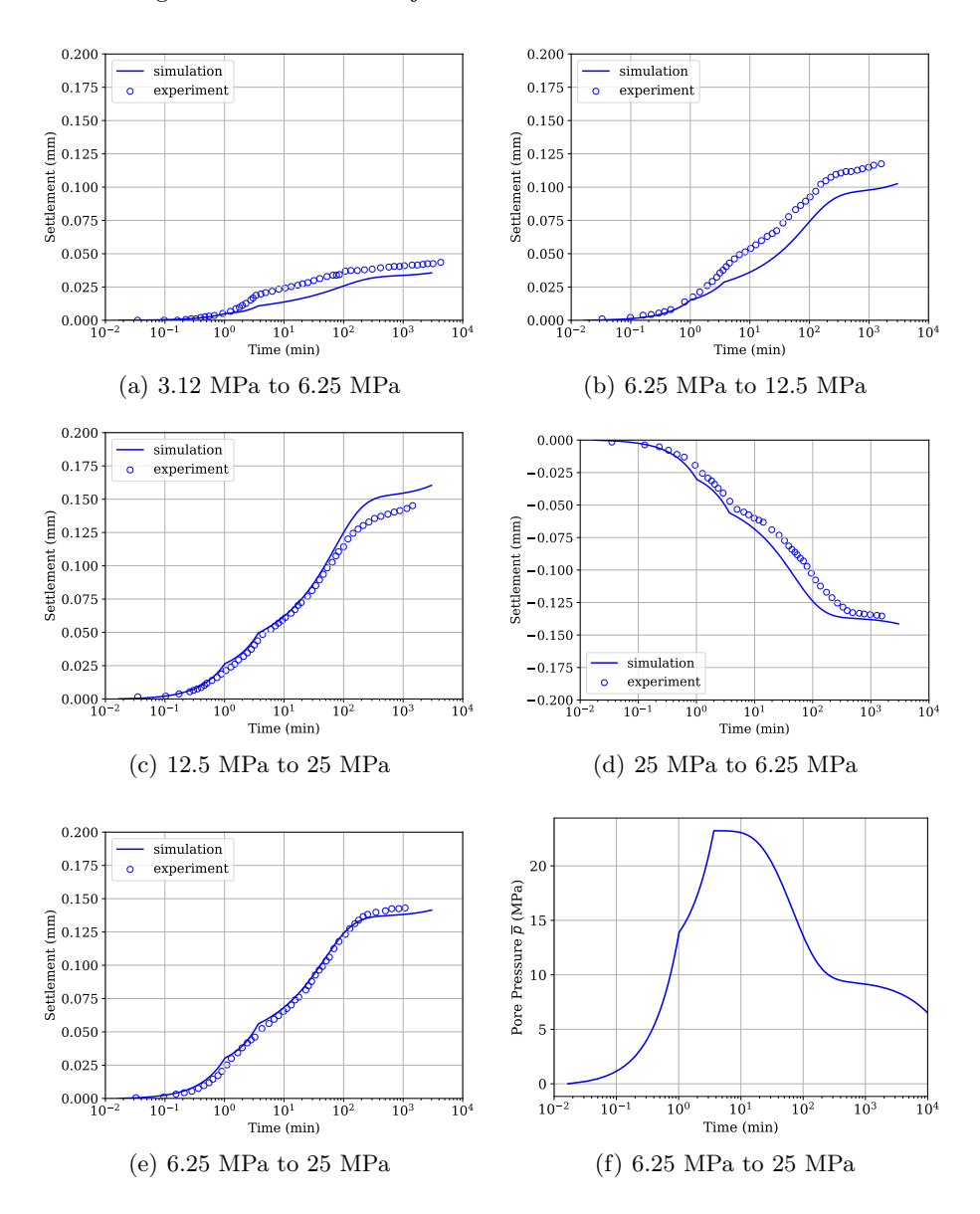


Fig. 4. Evolution of settlement and pore pressure with different load increments.

that the pore pressure distribution along the vertical centerline oscillates without stabilization. The solution with $\tau=1$ shows that the pore pressure oscillation is only partially suppressed, but with $\tau=10$ the oscillation completely disappears for both NC and OC simulations. Figure 7 portrays the spatial variation of p_m in the vicinity of the strip load with and without numerical

Table 2. Calibrated parameters for Opalinus clay shale.

| | Value | Unit |
|----------------------|-------|-----------------------|
| Elasticity: | | |
| λ | 429 | MPa |
| a | -27 | MPa |
| b | 1600 | MPa |
| μ_T | 2360 | MPa |
| μ_L | 1000 | MPa |
| Plasticity: | | |
| c_1 | 0.3 | - |
| c_2 | -1.3 | - |
| c_3 | 1.4 | - |
| M | 0.75 | - |
| λ_p | 0.014 | - |
| p_{c0} | -9 | MPa |
| Fluid flow: | | |
| κ_{\parallel} | 10 | nD |
| $\kappa_{\perp}^{"}$ | 3 | nD |
| κ_m | 0 | nD |
| μ_f | 1 | cP |
| \bar{k} | 1 | nD |
| $\bar{\alpha}$ | 5 | m^{-2} |
| $ ho_M$ | 1 | ton/m^3 |
| ρ_m | 1 | ton/m^3 |
| Others: | | |
| ϕ_M | 0.19 | - |
| ϕ_m | 0.01 | - |
| K_s | 13 | GPa |
| K_M | 2 | GPa |
| K_m | 2 | GPa |
| au | 10 | - |

stabilization. We remark that the peak values of the oscillation in the unstabilized solution could be large enough to compromise the accuracy of the solution.

Having calibrated the stabilization parameter at $\tau=10$, we now simulate the pore pressure dissipation under the same applied strip load of 1 MPa. The simulation consists of time stepping over 80 time steps with an initial time increment $\Delta t=25$ min and increasing each increment by a factor of 1.25 from its previous value, i.e., $\Delta t_{n+1}=1.25\Delta t_n$. For the following simulations, we first ignore the mass transfer of fluid between the macropores and micropores by setting $\bar{k}=0$, which is equivalent to treating the macropores and micropores as two independent flow channels. The results are compared with the response of a single-porosity medium with porosity equal to either that of the macropores or that of the micropores.

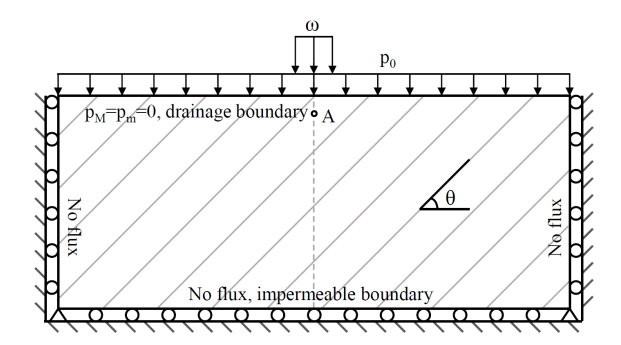


Fig. 5. Illustration of the consolidation problem.

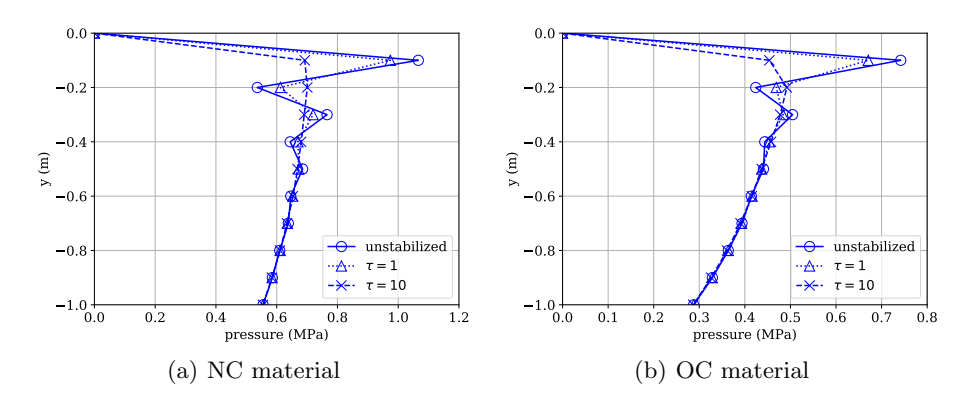


Fig. 6. Pressure distribution along the vertical center line with different stabilization parameter τ right after the strip load is applied.

To show that the proposed stabilization scheme works throughout the full range of drainage responses, the profile of the two pore pressures along the vertical centerline as well as the 2D spatial variation of p_m are shown in Figs. 8 and 9 after 10 time steps of consolidation, or around 0.6 day. For the macropore pressure p_M , no oscillation is observed even with the unstabilized solution, suggesting that numerical instability only manifests itself during undrained loading. Furthermore, the calculated values of p_M are nearly identical for both stabilized and unstabilized solutions, suggesting that the stabilization scheme does not impact the drained response. The plots also show that without numerical stabilization, the micropore pressure p_m overshoots near the drainage boundary. This phenomenon is due in part to the high gradient that exists near the drainage boundary and in part to inf-sup instability [106]. Interestingly, the stabilized solution appears to have suppressed this instability as well.

Figures 10 and 11 compare the pore pressure and ground settlement responses predicted by the single and double porosity theories. The pore pressure are pressured to the single and double porosity theories.

Table 3. Parameters used in the simulations.

| | Value | Unit |
|-----------------------|---------|--------------|
| Elasticity: | | |
| λ | 4270 | MPa |
| a | -1870 | MPa |
| b | 5420 | MPa |
| μ_T | 9360 | MPa |
| μ_L | 6510 | MPa |
| Plasticity: | | |
| c_1 | 0.7 | - |
| c_2 | -0.36 | - |
| c_3 | 0.6 | - |
| M | 1.07 | - |
| λ_p | 0.00013 | - |
| p_{c0} | -1, -2 | MPa |
| Fluid flow: | | |
| κ_\parallel | 1 | $\mu { m D}$ |
| κ_{\perp} | 0.1 | $\mu { m D}$ |
| κ_m | 1 | nD |
| μ_f | 1 | cP |
| $\frac{\mu_f}{ar{k}}$ | 1 | nD |
| $\bar{\alpha}$ | 10 | m^{-2} |
| $ ho_M$ | 1 | ton/m^3 |
| $ ho_m$ | 1 | ton/m^3 |
| Others: | | |
| ϕ_M | 0.1 | - |
| ϕ_m | 0.05 | - |
| K_s | 43 | GPa |
| K_M | 2 | GPa |
| K_m | 2 | GPa |

sures were calculated at point A on the centerline located 1 m below the ground (Figure 5), while the surface settlement was calculated in the middle of the strip load. In the two single-porosity simulations, the total porosity of the medium was assumed to be the same as that of the double-porosity medium but with the permeability properties of either those of the macropores or those of the micropores. Results show that the time histories of \bar{p} and the accompanying ground settlement lie in between the pore pressure and ground settlement time histories of the two single-porosity simulations. Note that the time history of \bar{p} exhibits two time scales (double S-shape), whereas those of the single-porosity simulations exhibit only one time scale. The time history of the micropore pressure p_m shows the familiar Mandel-Cryer effect, in which the values increase first and then decays to zero.

An interesting set of responses portrayed in Figure 10 is that the pore pressures predicted by the two pore systems are the same in the undrained

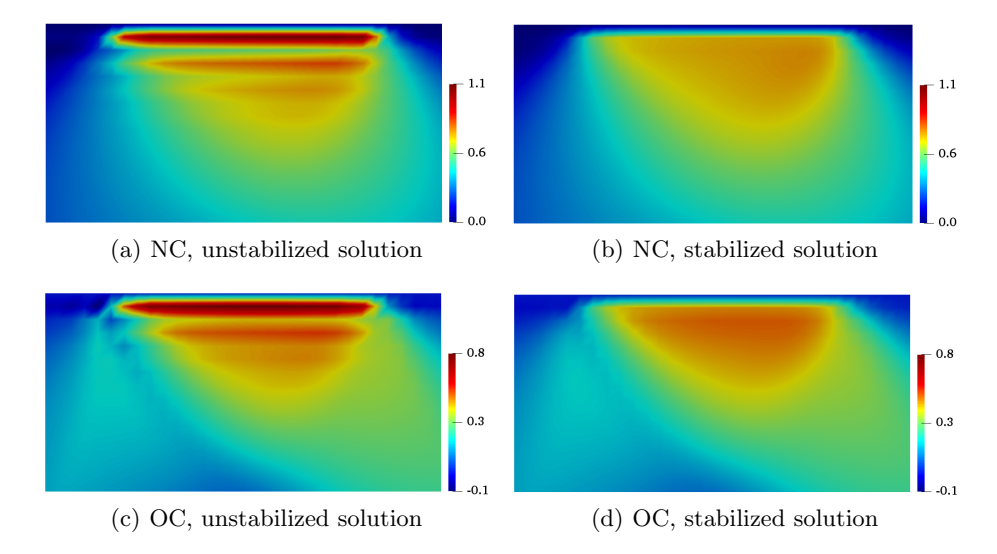


Fig. 7. Zoom of micropore pressure p_m in the vicinity of the strip load right after the strip load is applied. Left: unstabilized solution. Right: stabilized solution with $\tau = 10$. Color bars in MPa.

limit. This result can be verified by looking at the governing conservation laws, which are expressed as residual equations in (96) and (97). In the limit as $\Delta t \to 0$, only terms involving solid deformation and storage coefficients survive, which means that we are effectively solving the following equations:

$$\psi^{M} \boldsymbol{b} : \dot{\boldsymbol{\epsilon}}^{e} + \psi^{M} \mathbf{1} : \dot{\boldsymbol{\epsilon}}^{p} + S_{MM} \dot{p}_{M} + S_{Mm} \dot{p}_{m} = 0 \quad \text{in} \quad \mathcal{B},$$
 (99a)

$$\psi^m \mathbf{b} : \dot{\mathbf{c}}^e + \psi^m \mathbf{1} : \dot{\mathbf{c}}^p + S_{mM} \dot{p}_M + S_{mm} \dot{p}_m = 0 \quad \text{in} \quad \mathcal{B}.$$
 (99b)

Now, if the fluid in the two pore scales have the same stiffness, i.e., $K_M = K_m = K_f$, then we can add the two equations above to obtain

$$\boldsymbol{b} : \dot{\boldsymbol{\epsilon}}^e + \mathbf{1} : \dot{\boldsymbol{\epsilon}}^p + \frac{\dot{\overline{p}}}{m} = 0, \qquad (100)$$

where

$$\frac{1}{m} = \frac{\phi}{K_f} + \frac{\beta}{K_s} \tag{101}$$

and m is the Biot modulus defined in the single porosity formulation [117]. Thus, \bar{p} predicted via the double porosity formulation is the same as p predicted from the single porosity formulation in the undrained limit. Furthermore, dividing (99a) by ψ^M and (99b) by ψ^m and taking the difference yields

$$\frac{\phi}{K_f} (\dot{p}_M - \dot{p}_m) = 0, \qquad (102)$$

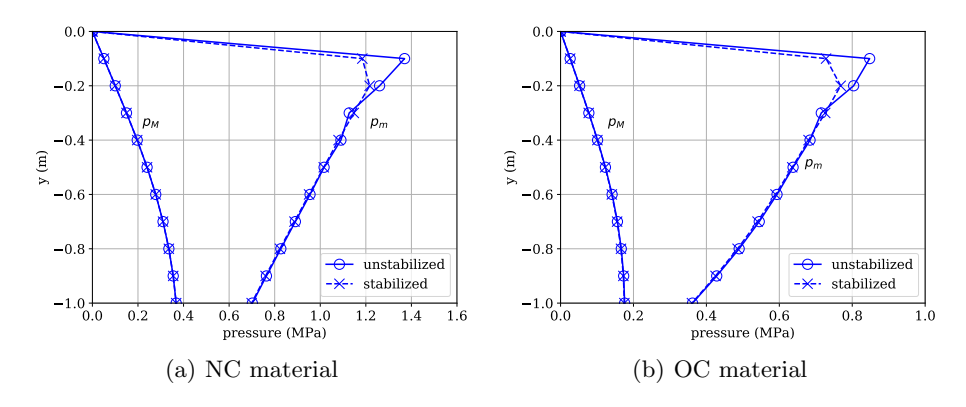


Fig. 8. Pressure distribution along the vertical center line after 10 steps (≈ 0.6 day) of consolidation. Color bars in MPa.

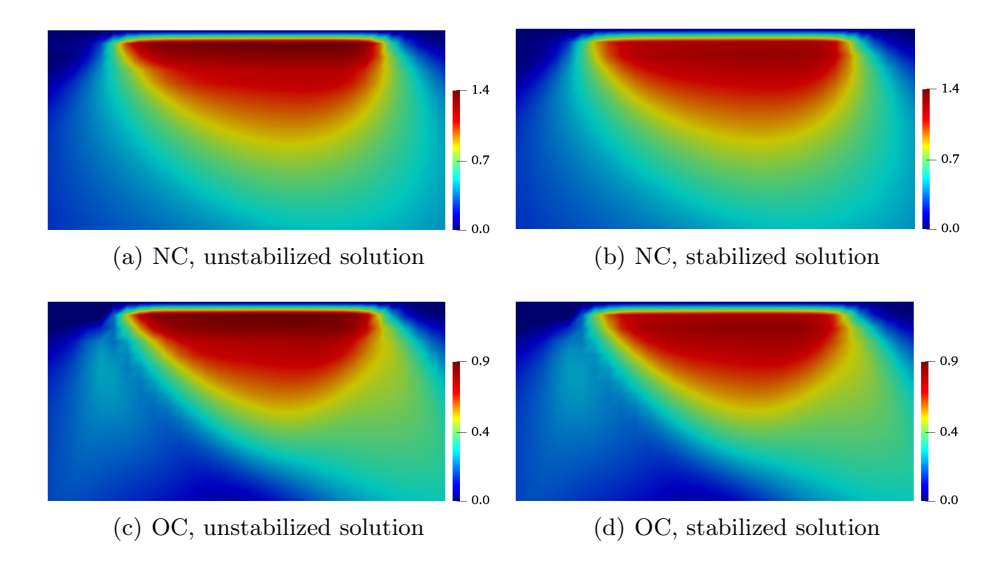


Fig. 9. Spatial variation of micropore pressure p_m after 10 steps (≈ 0.6 day) of consolidation. Left: unstabilized solution. Right: stabilized solution with $\tau = 10$. Color bars in MPa.

which implies that $p_m=p_M\equiv \overline{p}$ in the undrained limit.

Next, we investigate the impact of fluid mass transfer between the two pore scales during consolidation. Using the same parameters shown in Table 2, we reran the simulation with the fluid mass transfer turned on. The evolutions of pore pressure and ground settlement are shown in Figures 12 and 13, respectively. From these results, we see that consolidation now takes a shorter period of time to complete since the mass transfer mechanism pro-

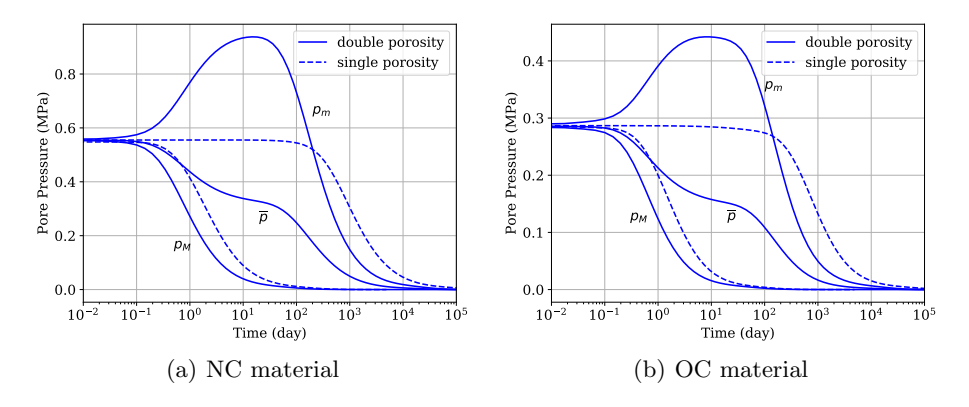


Fig. 10. Evolution of pore pressure at point A.

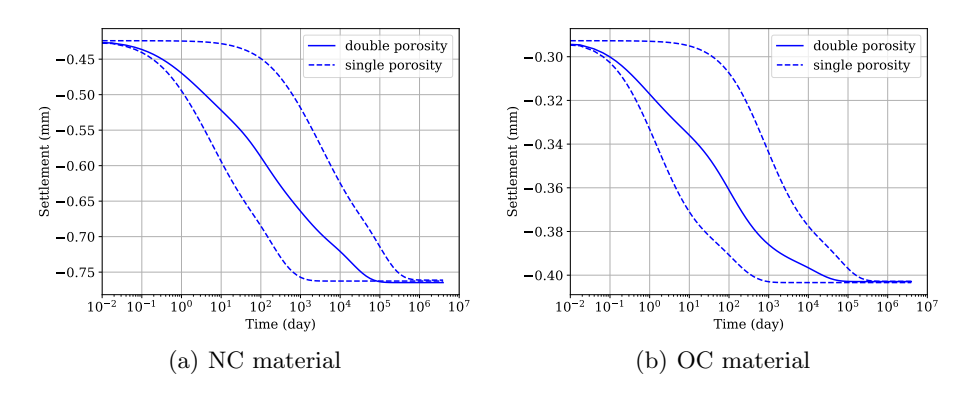


Fig. 11. Evolution of ground settlement.

vides another channel for the pore pressure in the micropores to dissipate. Also, because the macropores receives additional fluid from the micropores, it now takes longer for p_M to decay to zero. However, regardless of the fluid mass transfer, the ground settlement at the end of consolidation remains essentially the same.

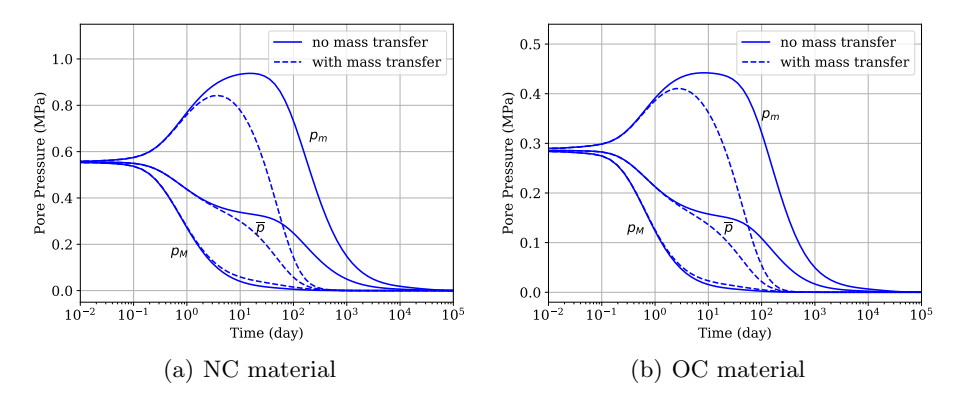


Fig. 12. Influence of fluid mass transfer on evolution of pore pressure at point A.

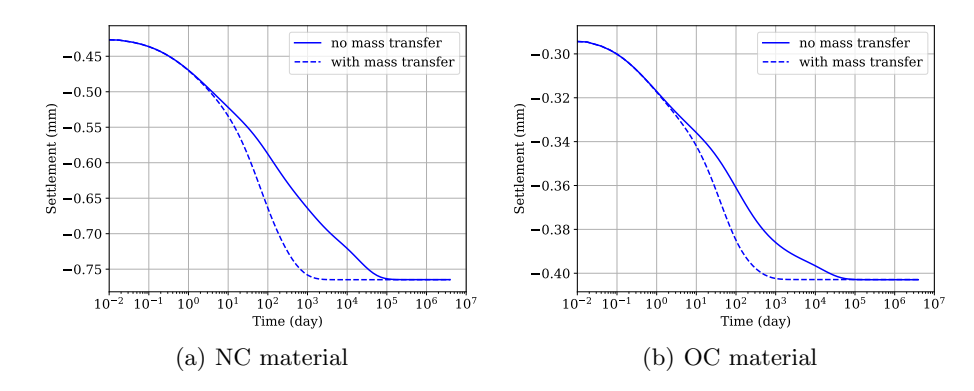


Fig. 13. Influence of fluid mass transfer on evolution of ground settlement.

Figures 14–17 show the spatial variations of pore pressures and Darcy velocities at two stages of consolidation in the NC and OC media. Note that even though we have assumed an isotropic permeability tensor for the micropores, the pore pressures and Darcy velocities at this pore scale still exhibit an asymmetric pattern with respect to the centerline, which can be attributed to the anisotropy of the material with respect to mechanical deformation. It is also interesting to note that even though the macropore pressure p_M has essentially dissipated at time t=56 days, the Darcy velocities at that pore scale remain higher than in the micropores, which implies that fluids in the micropores continue to drain into the macropores. This results in a faster overall consolidation of the porous medium.

Lastly, Figure 18 shows the spatial variation of plastic deformation in the NC and OC media at the end of consolidation. The patterns of localized plastic strain for both NC and OC simulations are similar to that predicted by the single porosity theory [117], in which a cone-shaped zone of plastic deformation forms beneath the strip load in the NC medium, while two conjugate plastic deformation bands form in the OC medium.

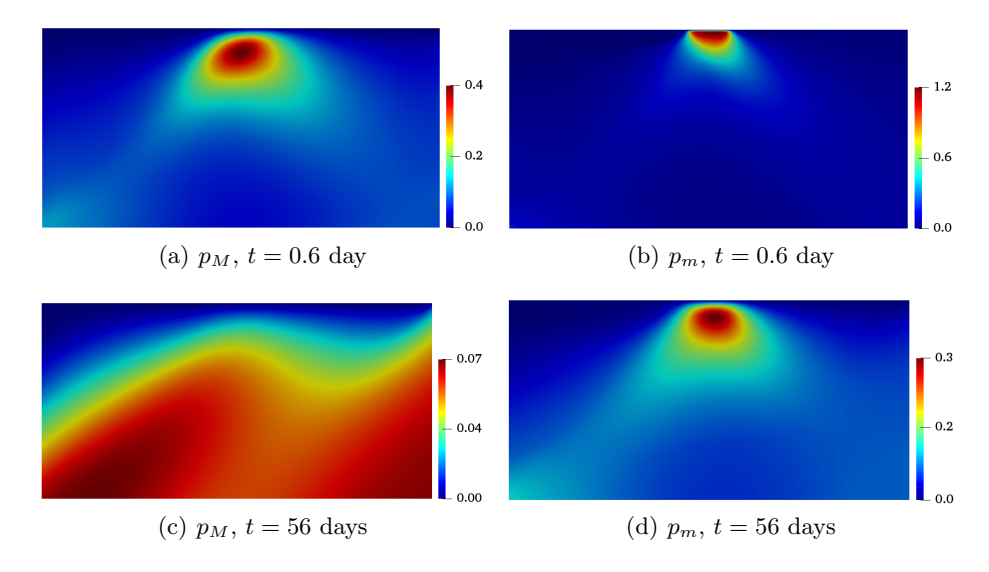


Fig. 14. Spatial variation of pore pressure for a NC medium after 10 time steps (≈ 0.6 day) and 30 time steps (≈ 56 days) of consolidation. Color bars in MPa.

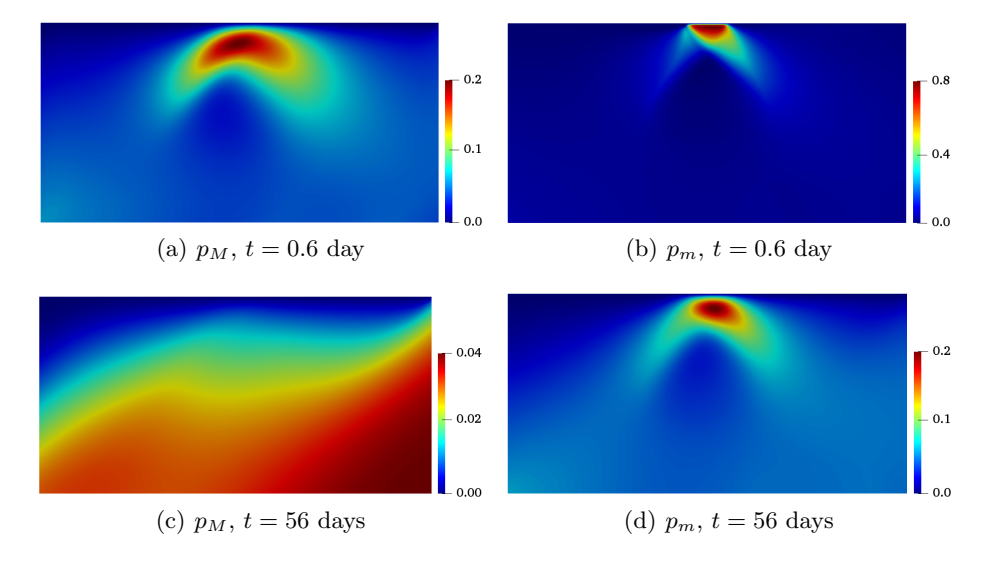


Fig. 15. Spatial variation of pore pressure for an OC medium after 10 time steps (≈ 0.6 day) and 30 time steps (≈ 56 days) of consolidation. Color bars in MPa.

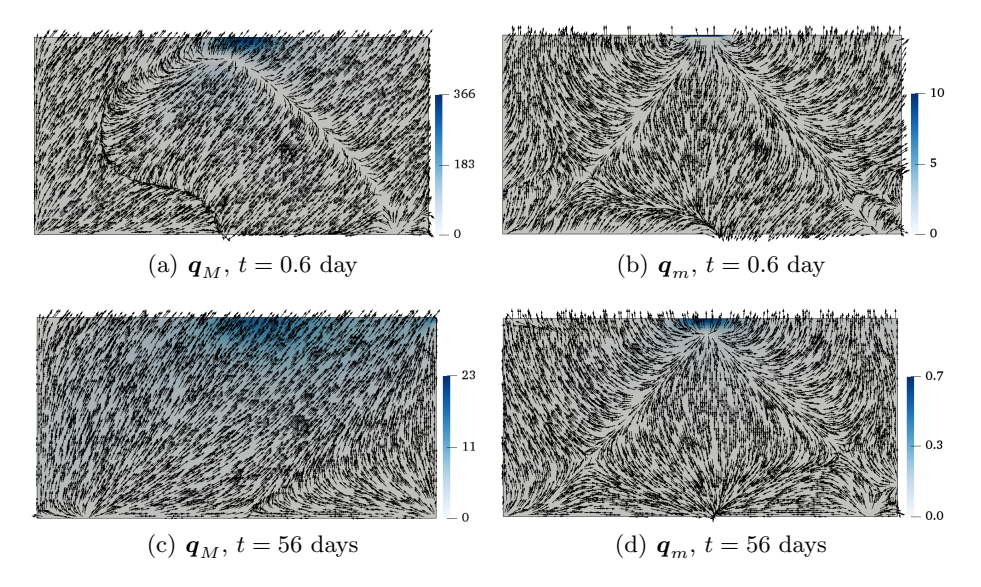


Fig. 16. Darcy velocity field in a NC medium after 10 time steps (≈ 0.6 day) and 30 time steps (≈ 56 days) of consolidation. Vectors are magnitudes of velocities in $\times 10^{-7}$ m/day.

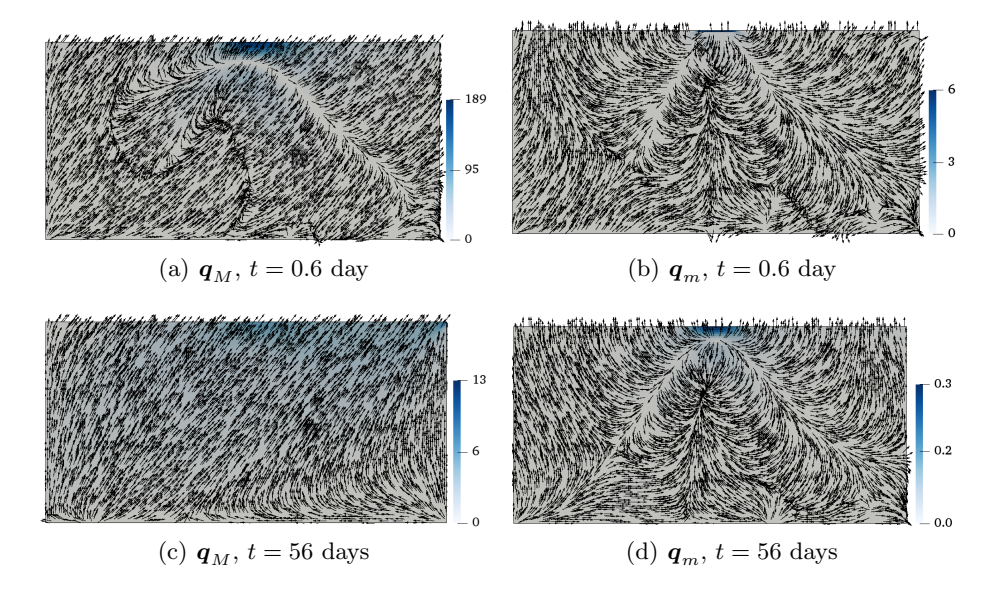


Fig. 17. Darcy velocity field in an OC medium after 10 time steps (≈ 0.6 day) and 30 time steps (≈ 56 days) of consolidation. Vectors are magnitudes of velocities in $\times 10^{-7}$ m/day.

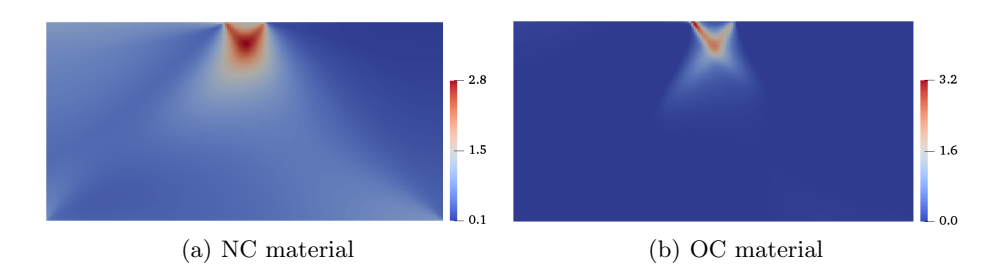


Fig. 18. Spatial variation of norm of plastic strain $\|\epsilon^p\|$ at end of consolidation. Color bars are strain norms in decimals $\times 10^{-4}$.

6 Conclusion

We have presented a thermodynamically consistent continuum framework for coupled fluid flow and solid deformation in anisotropic elastoplastic media with double porosity. Similar to the single porosity theory, two effective stress measures, σ' and σ'' , have been identified that are conjugate to the elastic

and plastic rates of deformation of the solid matrix, respectively. Stabilized low-order mixed finite elements have been employed to solve initial boundary-value problems, which alleviate the pore pressure oscillation due to inf-sup instability in the undrained limit while at the same time preserve the accuracy of the solution in the drained response.

The formulation has been used to simulate the one-dimensional consolidation of Opalinus Clay shale. With a single set of material parameters, the model has reproduced the compression-time history of this shale under different loading scenarios that included loading, unloading, and reloading. The formulation has also been used to simulate plane strain consolidation of a rectangular domain under a strip load to demonstrate the efficacy of the stabilization scheme in the undrained limit and the impacts of anisotropy, stress history, mass transfer, and the double porosity representation in general on the system response.

Some hydromechanical phenomena in science and engineering cannot be explained by single porosity theory alone, the most obvious one being the secondary consolidation exhibited by some porous geomaterials such as soils and rocks under one-dimensional constrained compression. The framework presented in this paper is a significant advance in the understanding of the impacts of anisotropy in the mechanical deformation and fluid flow properties on the response of materials with double porosity.

Acknowledgments

This material is based upon work supported by the U.S. Department of Energy, Office of Science, Office of Basic Energy Sciences, Geosciences Research Program, under Award Number DE-FG02-03ER15454. Support for materials and additional student hours were provided by the National Science Foundation under Award Number CMMI-1914780.

Appendix A: Derivation of the tangent matrix

The relationships below are used in the derivation:

$$\frac{\partial \boldsymbol{\sigma}''}{\partial \widetilde{\boldsymbol{\epsilon}}} = \mathbb{C}^{ag}, \quad \frac{\partial \widetilde{\boldsymbol{\epsilon}}}{\partial \boldsymbol{\epsilon}} = \mathbb{I}, \quad \frac{\partial \widetilde{\boldsymbol{\epsilon}}}{\partial p_{M}^{h}} = \psi^{M} \mathbb{C}^{e-1} : (\mathbf{1} - \boldsymbol{b}),
\frac{\partial \widetilde{\boldsymbol{\epsilon}}}{\partial p_{m}^{h}} = \psi^{m} \mathbb{C}^{e-1} : (\mathbf{1} - \boldsymbol{b}), \quad \frac{\partial \boldsymbol{\epsilon}^{e}}{\partial \boldsymbol{\epsilon}} = \mathbb{C}^{e-1} : \mathbb{C}^{ag},
\frac{\partial \boldsymbol{\epsilon}^{e}}{\partial p_{M}^{h}} = \psi^{M} (\mathbb{C}^{e-1} : \mathbb{C}^{ag} - \mathbb{I}) : \mathbb{C}^{e-1} : (\mathbf{1} - \boldsymbol{b}),
\frac{\partial \boldsymbol{\epsilon}^{e}}{\partial p_{m}^{h}} = \psi^{m} (\mathbb{C}^{e-1} : \mathbb{C}^{ag} - \mathbb{I}) : \mathbb{C}^{e-1} : (\mathbf{1} - \boldsymbol{b}),$$
(103)

The submatrix K_{ij} in the tangent matrix for Newton iteration is given as follows.

$$K_{11} = \frac{\partial \mathcal{R}_{u}}{\partial d} = \int_{\mathcal{B}} B^{T} \frac{\partial \sigma''}{\partial \bar{\epsilon}} : \frac{\partial \bar{\epsilon}}{\partial \bar{\epsilon}} B dV = \int_{\mathcal{B}} B^{T} e^{\alpha g} B dV, \qquad (104a)$$

$$K_{12} = \frac{\partial \mathcal{R}_{u}}{\partial p_{M}} = \int_{\mathcal{B}} B^{T} \frac{\partial \sigma''}{\partial \bar{\epsilon}} : \frac{\partial \bar{\epsilon}}{\partial p_{M}^{2}} N_{p} dV - \int_{\mathcal{B}} B^{T} \psi^{M} \mathbf{1} N_{p} dV + \int_{\mathcal{B}} N_{u}^{T} \frac{\partial \bar{\epsilon}}{\partial p_{M}} dV$$

$$= \int_{\mathcal{B}} B^{T} \psi^{M} [C^{\alpha g} : C^{\epsilon - 1} : (1 - b) - 1] N_{p} dV \qquad (104b)$$

$$+ \int_{\mathcal{B}} N_{u}^{T} \left(-\frac{\bar{\alpha} \bar{k} p_{M}}{\mu_{f} \phi^{M}} q_{M} N_{p} + \frac{\bar{\alpha} \bar{k} p_{m}}{\mu_{f} \phi^{m}} q_{m} N_{p} - \frac{c_{M}}{\phi^{M} \mu_{f}} \kappa_{M} E \right) dV,$$

$$K_{13} = \frac{\partial \mathcal{R}_{u}}{\partial p_{m}} = \int_{\mathcal{B}} B^{T} \frac{\partial \sigma'}{\partial \bar{\epsilon}} : \frac{\partial \bar{\epsilon}}{\partial p_{m}^{2}} N_{p} dV - \int_{\mathcal{B}} B^{T} \psi^{m} \mathbf{1} N_{p} dV + \int_{\mathcal{B}} N_{u}^{T} \frac{\partial \bar{c}}{\partial p_{m}} dV$$

$$= \int_{\mathcal{B}} B^{T} \psi^{m} [C^{\alpha g} : e^{\epsilon - 1} : (1 - b) - 1] N_{p} dV \qquad (104c)$$

$$+ \int_{\mathcal{B}} N_{u}^{T} \left(-\frac{\bar{\alpha} \bar{k} p_{m}}{\mu_{f} \phi^{m}} q_{m} N_{p} + \frac{\bar{\alpha} \bar{k} p_{M}}{\mu_{f} \phi^{M}} q_{M} N_{p} - \frac{c_{m}}{\phi^{m} \mu_{f}} \kappa_{m} E \right) dV,$$

$$K_{21} = \frac{\partial \mathcal{R}_{p_{M}}}{\partial d} = \int_{\mathcal{B}} N_{p}^{T} \psi^{M} 1 B dV + \int_{\mathcal{B}} N_{p}^{T} \left[\psi^{M} (b - 1) : \frac{\partial e^{\epsilon}}{\partial \epsilon} \right] B dV \qquad (104d)$$

$$= \int_{\mathcal{B}} N_{p}^{T} \psi^{M} \left[(b - 1) : C^{\epsilon - 1} : C^{\alpha g} + 1 \right] B dV,$$

$$K_{22} = \frac{\partial \mathcal{R}_{p_{M}}}{\partial p_{M}} = \int_{\mathcal{B}} \left(S_{MM} + \frac{\Delta t \bar{\alpha} \bar{k}}{\mu_{f}} \right) N_{p}^{T} N_{p} dV + \int_{\mathcal{B}} N_{p}^{T} \left[\psi^{M} (b - 1) : \frac{\partial e^{\epsilon}}{\partial \epsilon} \right] N_{p} dV$$

$$+ \int_{\mathcal{B}} \frac{\Delta t}{\mu_{f}} E^{T} \kappa_{M} E dV + \int_{\mathcal{B}} \left(S_{MM} + \frac{\Delta t \bar{\alpha} \bar{k}}{\mu_{f}} \right) N_{p}^{T} N_{p} dV + \int_{\mathcal{B}} \frac{\Delta t}{N_{p}^{T}} N_{p}^{T} V_{p}^{T} V_{p}^{T} N_{p}^{T} V_{p}^{T} V_{p}^{T} N_{p}^{T} V_{p}^{T} V_{p}^{T} V_{p}^{T} N_{p}^{T} V_{p}^{T} V$$

 $+ \int_{\mathbb{R}} \boldsymbol{N}_p^{\mathsf{T}} \left[(\boldsymbol{\psi}^m)^2 (\boldsymbol{b} - \boldsymbol{1}) : (\mathbb{C}^{e-1} : \mathbb{C}^{ag} - \mathbb{I}) : \mathbb{C}^{e-1} : (\boldsymbol{1} - \boldsymbol{b}) \right] \boldsymbol{N}_p dV$

 $+ \int_{\mathbb{R}} \frac{\Delta t}{K} \boldsymbol{N}_{p}^{\mathsf{T}} \boldsymbol{q}_{m} \boldsymbol{E} dV - \int_{\mathbb{R}} \frac{\Delta t}{K_{m} u} \boldsymbol{N}_{p}^{\mathsf{T}} \nabla p_{m}^{h} \cdot \boldsymbol{\kappa}_{m} \boldsymbol{E} dV.$

(104i)

References

- [1] Aifantis EC (1979) On the response of fissured rocks. *Developments in Mechanics* 10(1):249–253
- [2] Ashworth M, Doster F (2020) Anisotropic dual?continuum representations for multiscale poroelastic materials: Development and numerical modelling. *International Journal for Numerical and Analytical Methods* in Geomechanics. 44(17):2304–2328
- [3] Attewell PB, Sandford MR (1974) Intrinsic shear strength of a brittle, anisotropic rock—I: experimental and mechanical interpretation. *International Journal of Rock Mechanics and Mining Sciences and Geomechanics Abstracts* 11(11): 423–430
- [4] Bangerth W, Hartmann R, Kanschat G (2007) deal.II—A general-purpose object-oriented finite element library. ACM Transactions on Mathematical Software 33(4): Article 24
- [5] Barenblatt GI, Zheltov IP, Kochina IN (1960) Basic concepts in the theory of seepage of homogeneous liquids in fissured rocks [strata]. *Journal of Applied Mathematics and Mechanics* 24(5):1286–1303
- [6] Bennett KC, Berla LA, Nix WD, Borja RI (2015) Instrumented nanoindentation and 3D mechanistic modeling of a shale at multiple scales. Acta Geotechnica 10:1–14
- [7] Bennett KC, Regueiro RA, Borja RI (2016) Finite strain elastoplasticity considering the Eshelby stress for materials undergoing plastic volume change. *International Journal of Plasticity* 77:214–245
- [8] Bennett KC, Borja RI (2018) Hyper-elastoplastic/damage modeling of rock with application to porous limestone. *International Journal of Solids* and Structures 143:218–231
- [9] Berryman JG, Wang HF (2000) Elastic wave propagation and attenuation in a double-porosity dual-permeability medium. *International Journal of Rock Mechanics and Mining Sciences* 37(1–2):63–78
- [10] Bhandari AR, Flemings PB, Polito PJ, Cronin MB, Bryant SL (2015) Anisotropy and stress dependence of permeability in the Barnett shale. Transport in porous media 108(2):393–411
- [11] Bochev PB, Dohrmann CR (2006) A computational study of stabilized, low-order C0 finite element approximations of Darcy equations. *Computational Mechanics* 38(4–5):323–333
- [12] Boehler JP, Sawczuk (1977) On yielding of oriented solids. Acta Mechanica 27(1-4):185-204
- [13] Bonazzi A, Jha B, de Barros FPJ (2020) Transport analysis in deformable porous media through integral transforms. *International Journal for Numerical and Analytical Methods in Geomechanics*, https://doi.org/10.1002/nag.3150
- [14] Bonnelye A, Schubnel A, David C, Henry P, Guglielmi Y, Gout C, Fauchille AL, Dick P (2017) Strength anisotropy of shales deformed un-

- der uppermost crustal conditions. Journal of Geophysical Research: Solid Earth. 122(1):110–129
- [15] Borja RI, Tamagnini C, Alarcón E (1998) Elastoplastic consolidation at finite strain part 2: finite element implementation and numerical examples. Computer Methods in Applied Mechanics and Engineering 159(1– 2):103–122
- [16] Borja RI (2006). On the mechanical energy and effective stress in saturated and unsaturated porous continua. *International Journal of Solids and Structures* 43(6):1764–1786
- [17] Borja RI, Koliji A (2009) On the effective stress in unsaturated porous continua with double porosity. *Journal of the Mechanics and Physics of Solids* 57(8):1182–1193
- [18] Borja RI, Rahmani H (2012) Computational aspects of elasto-plastic deformation in polycrystalline solids. *Journal of Applied Mechanics* 79(3):031024
- [19] Borja RI (2013) Plasticity Modeling & Computation. Springer-Verlag, Berlin-Heidelberg.
- [20] Borja RI, Rahmani H (2014) Discrete micromechanics of elastoplastic crystals in the finite deformation range. Computer Methods in Applied Mechanics and Engineering 275:234–263
- [21] Borja RI, Choo J (2016) Cam-Clay plasticity, Part VIII: A constitutive framework for porous materials with evolving internal structure. Computer Methods in Applied Mechanics and Engineering 309:653–679
- [22] Borja RI, Yin Q, Zhao Y (2020) Cam-Clay plasticity. Part IX: On the anisotropy, heterogeneity, and viscoplasticity of shale. Computer Methods in Applied Mechanics and Engineering 360:112695
- [23] Bowen RM (1976) Theory of mixtures. In: A.C. Eringen (Ed.), Continuum Physics, Volume III Mixtures and EM Field Theories, Academic Press, New York. 1–127
- [24] Brace WF, Martin RJ (1968) A test of the law of effective stress for crystalline rocks of low porosity. In *International Journal of Rock Mechanics and Mining Sciences & Geomechanics Abstracts* 5(5):415–426
- [25] Bryant EC, Sun W (2018) A mixed-mode phase field fracture model in anisotropic rocks with consistent kinematics. Computer Methods in Applied Mechanics and Engineering 342:561–584
- [26] Bryant EC, Sun W (2019) A micromorphically regularized Cam-clay model for capturing size-dependent anisotropy of geomaterials. *Computer Methods in Applied Mechanics and Engineering*. 354:56-95
- [27] Camargo JT, White JA, Borja RI (2020) A macroelement stabilization for mixed finite element/finite volume discretizations of multiphase poromechanics. *Computational Geosciences* 1–18, https://doi.org/10.1007/s10596-020-09964-3
- [28] Castelletto N, White JA, Tchelepi HA (2015) Accuracy and convergence properties of the fixed-stress iterative solution of two-way cou-

- pled poromechanics. International Journal for Numerical and Analytical Methods in Geomechanics 39(14):1593–1618
- [29] Chalmers GR, Ross DJ, Bustin RM (2012) Geological controls on matrix permeability of Devonian Gas Shales in the Horn River and Liard basins, northeastern British Columbia, Canada. *International Journal of Coal Geology* 103:120–131
- [30] Charlet L, Alt-Epping P, Wersin P, Gilbert B (2017) Diffusive transport and reaction in clay rocks: A storage (nuclear waste, CO2, H2), energy (shale gas) and water quality issue. Advances in Water Resources 106:39– 59
- [31] Choo J, Borja RI (2015) Stabilized mixed finite elements for deformable porous media with double porosity. Computer Methods in Applied Mechanics and Engineering 293:131–154
- [32] Choo J, Sun W (2018) Coupled phase-field and plasticity modeling of geological materials: From brittle fracture to ductile flow. Computer Methods in Applied Mechanics and Engineering 330:1–32
- [33] Choo J, White JA, Borja RI (2016) Hydromechanical modeling of unsaturated flow in double porosity media. *International Journal of Geomechanics* 16(6):D4016002
- [34] Choo J, Semnani SJ, White JA (2020). An anisotropic viscoplasticity model for shale based on layered microstructure homogenization. arXiv preprint arXiv:2008.10910
- [35] Choo J (2019) Stabilized mixed continuous/enriched Galerkin formulations for locally mass conservative poromechanics. Computer Methods in Applied Mechanics and Engineering 357:112568
- [36] Coussy O (2004) Poromechanics. John Wiley & Sons.
- [37] Crisci E, Ferrari A, Giger SB, Laloui L (2019) Hydro-mechanical behaviour of shallow Opalinus Clay shale. Engineering Geology 251:214–227
- [38] Crook AJ, Yu JG, Willson SM (2002) Development of an orthotropic 3D elastoplastic material model for shale, in *SPE/ISRM Rock Mechanics Conference*, Irving, Texas.
- [39] Donath FA (1961) Experimental study of shear failure in anisotropic rocks. Geological Society of America Bulletin 72(6):985–989
- [40] Drescher A, Detournay E (1993) Limit load in translational failure mechanisms for associative and non-associative materials. *Géotechnique* 43(3):443–456
- [41] Duan K, Kwok CY, Pierce M (2016) Discrete element method modeling of inherently anisotropic rocks under uniaxial compression loading. International Journal for Numerical and Analytical Methods in Geomechanics 40(8):1150–1183
- [42] Elsworth D, Bai M (1992) Flow-deformation response of dual-porosity media. *Journal of Geotechnical Engineering* 118(1):107–124

- [43] Fávero Neto AH, Borja RI (2018) Continuum hydrodynamics of dry granular flows employing multiplicative elastoplasticity. Acta Geotechnica 13:1027-1040
- [44] Fávero Neto AH, Askarinejad A, Springman SM, Borja RI (2020) Simulation of debris flow on an instrumented test slope using an updated Lagrangian continuum particle method. *Acta Geotechnica* 15:2757–2777
- [45] Favero V, Ferrari A, Laloui L (2016) On the hydro-mechanical behaviour of remoulded and natural Opalinus Clay shale. *Engineering Geology* 208:128–135
- [46] Favero V, Ferrari A, Laloui L (2018) Anisotropic behaviour of Opalinus Clay through consolidated and drained triaxial testing in saturated conditions. Rock Mechanics and Rock Engineering 51(5):1305–1319
- [47] Ferrari A, Favero V, Laloui L (2016) One-dimensional compression and consolidation of shales. *International Journal of Rock Mechanics and Mining Sciences* 88:286–300
- [48] Gerke HH, Van Genuchten MT (1993) Evaluation of a first-order water transfer term for variably saturated dual-porosity flow models. Water Resources Research 29(4):1225–1238
- [49] Gray WG, Schrefler BA (2007) Analysis of the solid phase stress tensor in multiphase porous media. *International Journal for Numerical and Analytical Methods in Geomechanics* 31(4):541–581
- [50] Gray WG, Schrefler BA, Pesavento F (2009) The solid phase stress tensor in porous media mechanics and the Hill-Mandel condition. *Journal of the Mechanics and Physics of Solids* 57(3):539–554
- [51] Guo B, Bandilla KW, Nordbotten JM, Celia MA, Keilegavlen E, Doster F (2016) A multiscale multilayer vertically integrated model with vertical dynamics for CO₂ sequestration in layered geological formations. Water Resources Research 52(8):6490–6505
- [52] Guo B, Zheng Z, Bandilla KW, Celia MA, Stone HA (2016) Flow regime analysis for geologic CO₂ sequestration and other subsurface fluid injections. *International Journal of Greenhouse Gas Control* 53:284–291
- [53] Han B, Shen WQ, Xie SY, Shao JF (2019) Influence of pore pressure on plastic deformation and strength of limestone under compressive stress. *Acta Geotechnica* 14(2):535–545
- [54] Harris NB, Miskimins JL, Mnich CA (2011) Mechanical anisotropy in the Woodford Shale, Permian Basin: Origin, magnitude, and scale. The Leading Edge 30(3):284–291
- [55] Hashagen F, de Borst R (2001) Enhancement of the Hoffman yield criterion with an anisotropic hardening model. *Computers & Structures* 79(6):637–651
- [56] Hill R (1948) A theory of the yielding and plastic flow of anisotropic metals. Proceedings of the Royal Society of London. Series A. Mathematical and Physical Sciences 193(1033):281–297
- [57] Hoek E (1964) Fracture of anisotropic rock. Journal of the South African Institute of Mining and Metallurgy 64(10):501–523

- [58] Jaeger JC, Cook NG, Zimmerman R (2009) Fundamentals of rock mechanics, John Wiley & Sons
- [59] Jerman J, Mašín D (2020) Hypoplastic and viscohypoplastic models for soft clays with strength anisotropy. *International Journal for Numerical* and Analytical Methods in Geomechanics 44(10):1396–1416
- [60] Jha B, Juanes R (2007) A locally conservative finite element framework for the simulation of coupled flow and reservoir geomechanics. Acta Geotechnica 2:139–153
- [61] Khalili N, Valliappan S (1996) Unified theory of flow and deformation in double porous media. European Journal of Mechanics, A/Solids 15(2):321–336
- [62] Koliji A, Laloui L, Vulliet L (2010) Constitutive modeling of unsaturated aggregated soils. International Journal for Numerical and Analytical Methods in Geomechanics 34(17):1846–1876
- [63] Kwon O, Kronenberg AK, Gangi AF, Johnson B, Herbert BE (2004) Permeability of illite-bearing shale: 1. Anisotropy and effects of clay content and loading. *Journal of Geophysical Research: Solid Earth* 109(B10)
- [64] Li Z, Su G, Zheng Q, Nguyen TS (2020) A dual-porosity model for the study of chemical effects on the swelling behaviour of MX-80 bentonite. *Acta Geotechnica*. 15(3):635–653
- [65] Li C, Caner FC, Chau VT, Baant ZP (2017) Spherocylindrical microplane constitutive model for shale and other anisotropic rocks. *Journal of the Mechanics and Physics of Solids* 103:155–178
- [66] Li W, Rezakhani R, Jin C, Zhou X, Cusatis G (2017) A multiscale framework for the simulation of the anisotropic mechanical behavior of shale. International Journal for Numerical and Analytical Methods in Geomechanics 41(14):1494–1522
- [67] Liu C, Abousleiman YN (2020) Generalized solution to the anisotropic Mandel's problem. International Journal for Numerical and Analytical Methods in Geomechanics 44(17):2283–2303
- [68] Lo W, Borja RI, Deng JH, Lee JW (2020) Analytical solution of soil deformation and fluid pressure change for a two-layer system with an upper unsaturated soil and a lower saturated soil under external loading. *Journal of Hydrology* 588:124997
- [69] Loret B, Rizzi E (1999) Strain localization in fluid-saturated anisotropic elastic-plastic porous media with double porosity. *Journal of the Mechan*ics and Physics of Solids 47(3):503–530
- [70] Makhnenko RY, Labuz JF (2016) Elastic and inelastic deformation of fluid-saturated rock. Philosophical Transactions of the Royal Society A: Mathematical, Physical and Engineering Sciences 374(2078):20150422
- [71] Malvern LE (1969) Introduction to the Mechanics of a Continuous Medium. Prentice Hall, Inc., Englewood Cliffs, New Jersey
- [72] Mašín D (2013) Double structure hydromechanical coupling formalism and a model for unsaturated expansive clays. *Engineering Geology* 165:73–88

- [73] McLamore R, Gray KE (1967) The mechanical behavior of anisotropic sedimentary rocks. *Journal of Engineering for Industry* 89(1):62–73
- [74] Mohagheghian E, Hassanzadeh H, Chen Z (2019) CO2 sequestration coupled with enhanced gas recovery in shale gas reservoirs. *Journal of CO*₂ *Utilization* 34:646–655
- [75] Monforte L, Navas P, Carbonell JM, Arroyo M, Gens A (2019) Low-order stabilized finite element for the full Biot formulation in soil mechanics at finite strain. *International Journal for Numerical and Analytical Methods* in Geomechanics 43(7):1488–1515
- [76] Morgan SP, Einstein HH (2017) Cracking processes affected by bedding planes in Opalinus shale with flaw pairs. Engineering Fracture Mechanics 176:213–234
- [77] Mukherjee M, Nguyen GD, Mir A, Bui HH, Shen L, El-Zein A, Maggi F (2017) Capturing pressure- and rate-dependent behaviour of rocks using a new damage-plasticity model. *International Journal of Impact Engi*neering 110:208–218
- [78] Nasseri MHB, Rao KS, Ramamurthy T (2003) Anisotropic strength and deformational behavior of Himalayan schists. *International Journal of Rock Mechanics and Mining Sciences* 40(1):3–23
- [79] Nguyen VX, Abousleiman YN (2010) Poromechanics solutions to plane strain and axisymmetric Mandel-type problems in dual-porosity and dual-permeability medium. *Journal of Applied Mechanics* 77(1):011002
- [80] Niandou H, Shao JF, Henry JP, Fourmaintraux D (1997) Laboratory investigation of the mechanical behaviour of Tournemire shale. *Interna*tional Journal of Rock Mechanics and Mining Sciences 34(1):3–16
- [81] Nova R (1986) An extended Cam-Clay model for soft anisotropic rocks. Computers and Geotechnics 2(2):69–88
- [82] Pan Z, Ma Y, Connell LD, Down DI, Camilleri M (2015) Measuring anisotropic permeability using a cubic shale sample in a triaxial cell. Journal of Natural Gas Science and Engineering 26:336–344
- [83] Papadimitriou AG, Chaloulos YK, Dafalias YF (2019) A fabric-based sand plasticity model with reversal surfaces within anisotropic critical state theory. *Acta Geotechnica* 14(2):253–277
- [84] Parisio F, Laloui L (2017) Plastic-damage modeling of saturated quasibrittle shales. International Journal of Rock Mechanics and Mining Sciences 93:295–306
- [85] Ramamurthy T, Rao GV, Singh J (1993) Engineering behaviour of phyllites. Engineering Geology 33(3):209–225
- [86] Rice JC (1977) Pore pressure effects in inelastic constitutive formulations for fissured rock masses. In: Advances in Civil Engineering Through Engineering Mechanics 360–363, ASCE, New York
- [87] Sánchez M, Gens A, Villar MV, Olivella S (2016) Fully coupled thermohydro-mechanical double-porosity formulation for unsaturated soils. *International Journal of Geomechanics* 16(6):D4016015

- [88] Saurabh S, Harpalani S (2018) The effective stress law for stress-sensitive transversely isotropic rocks. *International Journal of Rock Mechanics and Mining Sciences* 101:69–77
- [89] Semnani SJ, Borja RI (2017). Quantifying the heterogeneity of shale through statistical combination of imaging across scales. Acta Geotechnica 12:1193–1205
- [90] Semnani SJ, White JA, Borja RI (2016) Thermoplasticity and strain localization in transversely isotropic materials based on anisotropic critical state plasticity. *International Journal for Numerical and Analytical Methods in Geomechanics* 40(18):2423–2449
- [91] Semnani SJ, White JA (2020). An Inelastic Homogenization Framework for Layered Materials with Planes of Weakness. *Computer Methods in Applied Mechanics and Engineering* 370:113221
- [92] Shen WQ, Shao JF (2018) A micro-mechanics-based elastic-plastic model for porous rocks: applications to sandstone and chalk. *Acta Geotechnica* 13(2):329–340
- [93] Sitarenios P, Kavvadas M (2020) A plasticity constitutive model for unsaturated, anisotropic, nonexpansive soils. *International Journal for Nu*merical and Analytical Methods in Geomechanics 44(4):435–454
- [94] Sone H, Zoback MD (2013) Mechanical properties of shale-gas reservoir rocks—Part 2: Ductile creep, brittle strength, and their relation to the elastic modulus. *Geophysics* 78(5):D393—D402
- [95] Song X, Ye M, Wang K (2017) Strain localization in a solid-water-air system with random heterogeneity via stabilized mixed finite elements. *International Journal for Numerical Methods in Engineering* 112(13):1926–1950
- [96] Suvorov AP, Selvadurai APS (2019) The Biot coefficient for an elastoplastic material. *International Journal of Engineering Science* 145:103166
- [97] Terzaghi K (1925) Erdbaumechanik auf bodenphysikalischer Grundlage. Franz Deuticke, Vienna, Austria
- [98] Terzaghi K (1943) Theoretical Soil Mechanics. John Wiley & Sons. New York, 11–15
- [99] Tjioe M, Borja RI (2015) On the pore-scale mechanisms leading to brittle and ductile deformation behavior of crystalline rocks. *International Journal for Numerical and Analytical Methods in Geomechanics* 39(11):1165–1187
- [100] Tjioe M, Borja RI (2016) Pore-scale modeling of deformation and shear band bifurcation in porous crystalline rocks. *International Journal for Numerical Methods in Engineering* 108(3):183–212
- [101] Ueda K, Iai S (2019) Constitutive modeling of inherent anisotropy in a strain space multiple mechanism model for granular materials. *International Journal for Numerical and Analytical Methods in Geomechanics* 43(3):708–737

- [102] Wang K, Sun W (2018) A multiscale multi-permeability poroplasticity model linked by recursive homogenizations and deep learning. Computer Methods in Applied Mechanics and Engineering 334:337–380
- [103] Wang K, Sun W (2019) An updated Lagrangian LBM-DEM-FEM coupling model for dual-permeability fissured porous media with embedded discontinuities. Computer Methods in Applied Mechanics and Engineering 344:276–305
- [104] Wang K, Song X (2020) Strain localization in non-isothermal unsaturated porous media considering material heterogeneity with stabilized mixed finite elements. Computer Methods in Applied Mechanics and Engineering 359:112770
- [105] Wang S, Feng Q, Zha M, Javadpour F, Hu Q (2018) Supercritical methane diffusion in shale nanopores: effects of pressure, mineral types, and moisture content. *Energy & Fuels* 32(1):169–180
- [106] White JA, Borja RI (2008) Stabilized low-order finite elements for coupled solid-deformation/fluid-diffusion and their application to fault zone transients. Computer Methods in Applied Mechanics and Engineering 197(49-50):4353-4366
- [107] White JA, Borja RI (2011) Block-preconditioned Newton-Krylov solvers for fully coupled flow and geomechanics. *Computational Geosciences* 15(4):647
- [108] Wilson RK, Aifantis EC (1982) On the theory of consolidation with double porosity. *International Journal of Engineering Science* 20(9):1009– 1035
- [109] Wu YS (2002) Numerical simulation of single-phase and multiphase non-Darcy flow in porous and fractured reservoirs. *Transport in Porous Media* 49(2):209–240
- [110] Yang Z, Liao D, Xu T (2020) A hypoplastic model for granular soils incorporating anisotropic critical state theory. *International Journal for Numerical and Analytical Methods in Geomechanics* 44(6):723–748
- [111] Xie SY, Shao JF (2012) Experimental investigation and poroplastic modelling of saturated porous geometrials. *International Journal of Plasticity* 39:27-45
- [112] Xu L, Wong H, Fabbri A, Champir F, Branque D (2018) Modelling the poroplastic damageable behaviour of earthen materials. *Materials and Structures* 51(4):112
- [113] Zhang Q, Choo J, Borja RI (2019) On the preferential flow patterns induced by transverse isotropy and non-Darcy flow in double porosity media. Computer Methods in Applied Mechanics and Engineering 353:570–592
- [114] Zhang Q, Su Y, Wang W, Lu M, Sheng G (2018) Gas transport behaviors in shale nanopores based on multiple mechanisms and macroscale modeling. *International Journal of Heat and Mass Transfer* 125:845–857

- [115] Zhao Y, Semnani SJ, Yin Q, Borja RI (2018) On the strength of transversely isotropic rocks. *International Journal for Numerical and Analytical Methods in Geomechanics* 42(16):1917–1934
- [116] Zhao Y, Borja RI (2019) Deformation and strength of transversely isotropic rocks. In: *Desiderata Geotechnica* 237–241
- [117] Zhao Y, Borja RI (2020) A continuum framework for coupled solid deformation-fluid flow through anisotropic elastoplastic porous media. Computer Methods in Applied Mechanics and Engineering 369:113225
- [118] Zheng H, Shi AF, Liu ZF, Wang XH (2020) A dual-porosity model considering the displacement effect for incompressible two-phase flow. International Journal for Numerical and Analytical Methods in Geomechanics 44(5):691–704
- [119] Zhou J, Xie S, Jiang Y, Xian X, Liu Q, Lu Z, Lyu Q (2018) Influence of supercritical CO₂ exposure on CH₄ and CO₂ adsorption behaviors of shale: implications for CO₂ sequestration. *Energy & Fuels* 32(5):6073–6089